https://doi.org/10.5194/acp-2019-498
Preprint. Discussion started: 17 July 2019

Atmospheric Chemistry and Physics Discussions

The role of plume-scale processes in long-term impacts of aircraft emissions

Thibaud M. Fritz, Sebastian D. Eastham, Raymond L. Speth, and Steven R.H. Barrett

Laboratory for Aviation and the Environment, Department of Aeronautics and Astronautics, Massachusetts Institute of Technology, Cambridge, MA 02139, USA

Correspondence to: S.D. Eastham (seastham@mit.edu)

https://doi.org/10.5194/acp-2019-498
Preprint. Discussion started: 17 July 2019

Atmospheric Chemistry and Physics Discussions

Abstract. Emissions from aircraft engines contribute to atmospheric NO_x, driving changes in both the climate and in surface air quality. Existing atmospheric models typically assume instant dilution of emissions into large-scale grid cells, neglecting non-linear, small-scale processes occurring in aircraft wakes. They also do not explicitly simulate the formation of ice crystals, which could drive local chemical processing. This assumption may lead to errors in estimates of aircraft-attributable ozone production, and in turn to biased estimates of aviation's current impacts on the atmosphere and the effect of future changes in emissions. This includes soot emissions, on which contrail ice forms. These emissions are expected to reduce as biofuel usage increases, but their chemical effects are not well captured by existing models.

To address this problem, we develop a Lagrangian model which explicitly models the chemical and microphysical evolution of an aircraft plume. It includes a unified tropospheric-stratospheric chemical mechanism that incorporates heterogeneous chemistry on background and aircraft-induced aerosols. Microphysical processes are also simulated, including the formation, persistence, and chemical influence of contrails. The plume model is used to quantify how the long-term (24-hour) atmospheric chemical response to an aircraft plume varies in response to different environmental conditions, and engine characteristics, and fuel properties. We find that an instant dilution model consistently overestimates ozone production compared to the plume model, up to a maximum error of ~200% at cruise altitudes. Instant dilution of emissions also underestimates the fraction of remaining NO_x, although the magnitude and sign of the error vary with season, altitude, and latitude. We also quantify how changes in soot emissions affect plume behavior. Our results show that a 50% reduction in black carbon emissions, as may be possible through blending with certain biofuels, leads to contrails which evaporate ~9% faster and are 14% optically thinner. The conversion of emitted NO_x to HNO_3 and N_2O_5 falls by 65% and 69% respectively, resulting in chemical feedbacks which are not resolved by instant-dilution approaches. The persistent discrepancies between results from the instant dilution approach and from the aircraft plume model demonstrate that a parametrization of effective emission indices should be incorporated into 3-D atmospheric chemistry transport models.

1 Introduction

Worldwide air passenger traffic is projected to grow at an annual rate of 5% over the next two decades (Airbus, 2017; Boeing, 2017). Commercial aviation fuel usage has continuously increased (Mazraati, 2010) as demand for air transport has outpaced improvements in efficiency (Lee et al., 2001). Combined with difficulties in reducing emissions of pollutants such as nitrogen oxides (NO_x) from aircraft engines, aviation has a unique and growing influence on the chemical composition of the atmosphere.

The release of chemically reactive substances from aircraft exhausts induces perturbations in the environmental chemical balance that can persist for days (Meijer, 2001). Additionally, aviation is a unique sector in terms of its environmental challenges as it is the only direct, significant anthropogenic source of pollution at high altitude (8-12 km). Nitrogen oxides (NO_x = NO + NO_2) released from aircraft engines have been estimated to increase ozone concentrations in the Northern hemisphere by 2 to 9% (Penner, 1999; Schumann, 1997; Brasseur et al., 1996), while the ice clouds which form in aircraft exhausts ("contrails") have been estimated as having climate impacts of the same order of magnitude as the carbon-dioxide released in the plume (Kärcher, 2018).

The chemical effects of these emissions are typically simulated using global, Eulerian, 3-D atmospheric chemistry transport models. These models simulate aircraft exhaust as being released instantaneously into homogeneously-mixed grid cells which are orders of magnitude larger than the aircraft plume (Brasseur et al., 1998; Meijer et al., 2000; Eyring et al., 2007). This approach does not explicitly capture the high initial species concentrations within the plume, including the effects of non-linear chemistry in the early stages or the formation (and chemical effects) of local aerosol clouds including contrails. Shortly after release into the atmosphere, species concentrations in the aircraft plume can be several orders of magnitude larger than their background levels. NO_x concentrations at cruise altitude can exceed values up to 20 ppbv in the early stages of the plume, whereas background NO_x levels are typically between 0.007 ppbv and 0.15 ppbv in flight corridor such as the North Atlantic Flight Corridor (NAFC) (Schumann et al., 1998). Previous studies which have explicitly modeled the gas-phase components of the plume have shown that the "instant dilution" approach results in inaccurate estimation of the plume's chemical effects on the environment (Petry et al., 1998; Kraabøl et al., 2000; Cariolle et al., 2009). Furthermore, the effects of interactions between contrail ice and the plume chemistry - including as a surface for rapid heterogeneous chemistry - have not yet been quantified.

Field measurements over the past decades, such as the SUCCESS (Toon and Miake-Lye, 1998), POLINAT (Schumann et al., 2000) and SULFUR experiments (Schumann et al., 2002), have measured the microphysical characteristics of both liquid aerosol and ice particles (contrails) in aircraft plumes. Contrail modeling efforts based on these measurements have shown that these aerosols are sensitive to ambient relative humidity, fuel sulfur content, and the amount of emitted solid particles (Kärcher, 1998; Wong and Miake-Lye, 2010). In the early stages, non-volatile aerosols take up a significant amount

https://doi.org/10.5194/acp-2019-498
Preprint. Discussion started: 17 July 2019

Atmospheric Chemistry and Physics Discussions

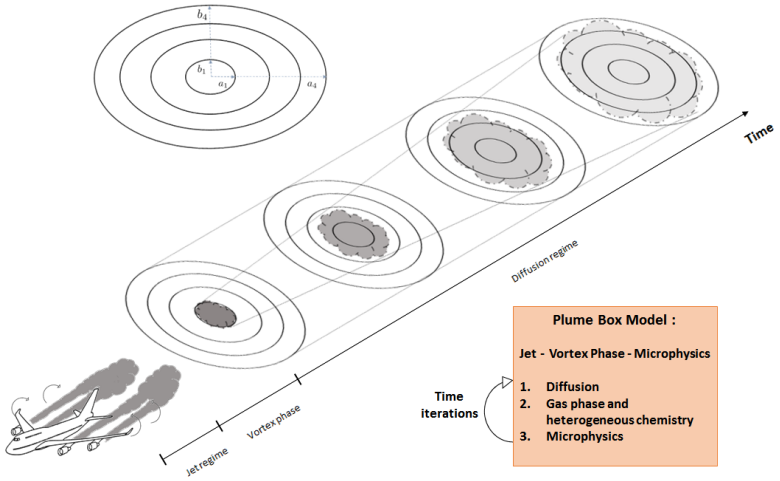

Figure 1. Schematic of the discretized ring approach used in APCEMM. The rings' major and minor axis are denoted by a_i and b_i respectively.

of the emitted water vapor through condensation and heterogeneous freezing, potentially leading to the formation of liquid aerosols and ice crystals. During the plume expansion regime, gas species react and diffuse, potentially reacting with one another through heterogeneous chemistry on their surface. This suggests that the formation of ice in aircraft exhausts may result in additional chemical processing which is not captured in either global atmospheric models or gas-phase aircraft plume models.

This gap also affects assessment of new fuels for aviation. Biofuels have been identified as an option to reduce aviation's climate impacts by reducing the net contribution of aviation to atmospheric CO_2. However, several of these alternative fuels are also expected to produce less soot (Speth et al., 2015) and to have a lower sulfur content (Gupta et al., 2010). The effect that these changes will have on aircraft plume chemistry and contrail evolution - and therefore on the total environmental impact of aircraft emissions - depend on the microphysical response of the plume. As such, the atmospheric effects of changing from conventional jet fuel to alternative fuels are not yet fully understood.

To address these issues we develop the Aircraft Plume Chemistry, Emissions, and Microphysics Model (APCEMM). APCEMM is applied under a variety of conditions to simulate the influence of changes in environment, aircraft characteristics, and fuel properties on in-plume chemistry and microphysics. Finally, the effects these changes are presented in terms of their impact on large-scale properties such as net 24-hour ozone production, end-of-lifetime NO_x partitioning, and contrail optical thickness.

2 Methods

We first describe the overall modeling approach used by APCEMM to simulate the chemistry and physics of an aircraft plume (sections 2.1). Sections 2.2 and 2.3 describe the details of the different models used for the initial and mature plume evolution phases, respectively. Finally, section 2.4 describes the experimental design used to determine the overall impact of plume-scale processes on long-term aircraft emissions impacts.

2.1 Model overview

APCEMM models the growth and chemical evolution of a single aircraft plume. Chemical concentrations and aerosol characteristics are calculated for a 2-D cross-section of the plume, perpendicular to the flight path. Dynamics, chemistry, and microphysics are explicitly modelled within the plume, using two different approaches depending on the age of the plume.

Observations and high-resolution modeling of aircraft wakes has shown three dynamical regimes in the first few minutes after emission, before the wake develops into a "mature" plume (Figure 1). Typical timescales and dilution ratios for an aircraft plume are shown in Table 1.

https://doi.org/10.5194/acp-2019-498
Preprint. Discussion started: 17 July 2019

Atmospheric Chemistry and Physics Discussions

Table 1. Plume timescales and dilution ratios (Kärcher, 1995). Dilution ratios are the ratio of the initial plume air mass to the air mass at the target time.

	Early-plume model			Long-term plume model
Phases	Early Jet Regime	Jet Regime	Vortex Regime	Diffusion Regime
Timescale	0.1 s	10 s	100 s	Few hours up to a day
Dilution ratio at end of phase [-]	5.5×10^{-1}	2.6×10^{-3}	9.9×10^{-4}	$< 1.0 \times 10^{-4}$

During the initial "early jet"and "jet" regimes, compressibility effects arise from the momentum-driven jet that last for a short amount of time of the order of a few seconds (Kärcher, 1995). After ~10 seconds the wing-tip vortices have formed and begin to affect the emissions plume. During this "vortex regime", the plume descends by distances of the order of several hundred meters (Kärcher, 1995; Schumann, 2012). Over the period of these three initial regimes, the plume cools rapidly to ambient temperatures (~280 K) from an initial temperature of 500-600 K, leading to a spike in ice and liquid water saturations approximately 100 ms after emission and triggering a range of microphysical processes (Kärcher et al., 2015). During this period, formation of sulfate aerosols, freezing on solid nuclei, condensation, heterogeneous nucleation, and coagulation also occur. Homogeneous freezing is not included. Previous studies have suggested that homogeneous freezing is unlikely in aircraft plumes given the number of pre-existing nuclei (Wong and Miake-Lye, 2010). This is because combustion particles can acquire an ice coating at temperatures much warmer than cruise temperatures, implying that ice crystals formed in the vicinity of the engines freeze by virtue of heterogeneous nucleation. In APCEMM, the plume is assumed to be well mixed during these first three regimes - the "early plume phase" (section 2.2).

The output of this box model is then provided as the initial condition for the model of the long term diffusion regime 2.3). This regime begins when viscous dissipation of turbulent energy causes the vortices to break apart. In this regime, the plume expands in ambient air. The rate of diffusion is controlled by the vertical stratification of the atmosphere and by the vertical gradient of the wind speed (wind shear). Unlike the early plume phase, spatial heterogeneity of the plume is explicitly accounted for in APCEMM during the diffusion regime, allowing for cross-plume concentration gradients.

2.2 Modeling of the early plume

During the early plume phase, the plume is treated as a single, well-mixed air mass. The air mass grows, dilutes, and cools through turbulent mixing with ambient air (entrainment). It also sinks and heats up due to the effect of the aircraft wing-tip vortices (vortex sinking). Throughout this phase we simulate rapid chemical changes, including the formation of liquid and solid aerosols.

2.2.1 Dilution and temperature evolution of the early plume

In the jet and vortex regimes, we adopt a formulation similar to the box model used in Kärcher (1995). The rate of change of chemical concentrations within the plume is dominated in this regime by dilution due to turbulent mixing. The contribution of wake mixing is approximated as a first-order decay term proportional to a time-dependent entrainment rate, i.e. $\omega_C(t)$.

$$\left(\frac{DC_k}{Dt}\right)\Big|_{\text{mix}} = -\omega_{C_k}(t)(C_k - C_{\text{Amb},k}), \tag{1}$$

where C_k is the molecular concentration of species k.

This entrainment rate agrees with the experimental data and curve fit provided in Schumann et al. (1998) for times greater than 1 s. $C_{\text{Amb},k}$ is the ambient molecular concentration of species k and is assumed to be constant during the jet and vortex regimes considering that the timescale associated with gas-phase chemistry is much greater than the time taken to reach the

https://doi.org/10.5194/acp-2019-498
Preprint. Discussion started: 17 July 2019

Atmospheric Chemistry and Physics Discussions

Table 2. Assumed conversion efficiencies of NO_x and SO_2 to secondary species

NO	→	HONO	1.5%
NO_2	→	HNO_3	4.0%
SO_2	→	H_2SO_4	0.5%
OH	→	H_2O_2	2.0%

diffusion regime. We assume that, during this time, gas-phase chemistry does not influence the concentrations of most species within the plume. The only exceptions are conversion of S(IV) to S(VI) and NO_x to HONO and HNO_3 as described in section 2.2.2, which evolve on similar timescales due to high initial concentrations (Kärcher et al., 1996).

The temperature of the plume during this initial phase is controlled by two processes. Firstly, prior experiments have shown that typical Lewis numbers are close to unity in coaxial jets, such as aircraft plumes (Forstall and Shapiro, 1950). Mixing of cold air with the hot exhaust stream (cooling the plume) is therefore assumed to occur at the same rate as entrainment of ambient chemical species. Secondly, the downward motion induced by the wing tip vortices also causes the air to heat up adiabatically, independently of the local lapse rate (Unterstrasser et al., 2008). The plume temperature evolution is therefore expressed as the sum of a positive heating due to vortex sinking and a first-order decay term representing entrainment, i.e.

$$\frac{dT_p}{dt} = \Gamma_d v_z - \omega_T(t)(T_p - T_{\mathrm{Amb}}(z)), \tag{2}$$

where T_p is the plume temperature in K, Γ_d the adiabatic lapse rate expressed in K/m, v_z the vertical velocity in m/s of the plume and T_{Amb} the ambient temperature in K evaluated as a function of the ambient lapse rate, which has been obtained as a function of latitude and altitude from monthly-averaged meteorological data obtained from the Modern-Era Retrospective analysis for Research and Applications, Version 2 (MERRA-2). The plume acquires a vertical motion during the vortex regime such that v_z is assumed to be non-zero only between the time at which the vortices start inducing a vertical displacement of the plume and the vortex break-up time. The wake vortex sinking is computed according to a parametric formulation described in Schumann (2012) from which we evaluate the mean downward displacement as a function of aircraft and ambient atmospheric characteristics.

2.2.2 Chemical conversions in the early plume

In the early stages of the plume, oxidation of NO and NO_2 results in the formation of HONO and HNO_3. Similarly, S(IV) undergoes oxidation to gaseous S(VI). As described in Kärcher (1999), conversion efficiencies of NO, NO_2 and SO_2 depend on the exit plane hydroxyl radical concentration. Tremmel et al. (1998) inferred initial OH concentrations at the combustor and engine exit through measurements of NO, HONO, HNO_3 as well as CO_2 to account for plume dilution. Their results indicate that the OH emission index ranges between 0.32 and 0.39 g (kg fuel)$^{-1}$ for the JT9D-7A, which corresponds to an engine exit mixing ratio lying between 9.0 and 14.4 ppmv. Conversion efficiencies used in APCEMM are depicted in Table 2. Even though the conversion efficiencies remain of the order of a few percent, they increase monotonically with the OH engine exit mixing ratio, as more radicals are available for the following reactions (Kärcher et al., 1996).

$$\mathrm{NO} + \mathrm{OH} \rightarrow \mathrm{HONO}$$
$$\mathrm{NO_2} + \mathrm{OH} \rightarrow \mathrm{HNO_3}$$
$$\mathrm{OH} + \mathrm{OH} \rightarrow \mathrm{H_2O_2}$$

2.2.3 Microphysical representation of the early plume

As the plume cools down and mixes with ambient air, aerosols begin to form, supplementing those which were emitted directly from the engine (e.g. soot particles). This both modifies the local chemical concentrations and changes the initial aerosol size distribution during the second phase of the plume. Four microphysical processes are explicitly considered: freezing of liquid particles into solid ones, condensation of gas onto liquid particles, nucleation of new liquid particles, and coagulation of both solid and liquid particles.

https://doi.org/10.5194/acp-2019-498
Preprint. Discussion started: 17 July 2019

Atmospheric Chemistry and Physics Discussions

We first consider growth of an existing particle population. The mathematical formulation is given in detail in Appendix A, but is covered briefly here. The microphysical model for growth of ice particles is adapted from Kärcher (1998). Solid particles (soot and metal) emitted by the aircraft serve as condensation nuclei for water vapor. Under supersatured conditions, deposition and sublimation induce ice crystal growth, depleting gaseous water vapor. During this initial phase, ice crystals are treated as mono-disperse (single size) and are assumed to be spherical. Under these assumptions, we need only consider the growth of a single "representative" particle, rather than considering the population as a whole. Because of the low ambient temperatures, water that condenses is assumed to freeze instantaneously, such that ice crystals grow by deposition of water molecules onto their surface. The rate of change in the ice mass of a particle, m_p, is then given by

$$\frac{dm_p}{dt} = H_p^{\text{act}}(m_p) \times 4\pi C_p D_{\text{v,eff}} \left(P_{\text{H}_2\text{O}} - P_{\text{H}_2\text{O}}^{\text{sat}}\right), \tag{3}$$

where $H_{\text{p}}^{\text{act}}$ is a function accounting for nucleus activation (equation A3), C_p is the ice crystal capacitance (equal to the particle radius r_p for spherical nuclei), $D_{\text{v,eff}}$ is the effective water vapor diffusion coefficient in air (equation A4), and $P_{\text{H}_2\text{O}}$ the water partial pressure. Assuming that each ice particle is nucleated on a soot particle with a dry radius of 20 nm, and using a fixed mass density for ice of 916.7 kg/m^3, this calculation also gives the rate of change of radius of solid particles in the plume. Calculation of each of the terms in equation 3 is described in Appendix A1.

Soot and ice particles can also grow by condensation of water vapor, sulfuric acid, and nitric acid into a partial liquid surface layer. The growth of this layer is related to the condensation (or evaporation) rate of H_2O, H_2SO_4 and HNO_3, calculated as

$$\frac{dN_{k,p}}{dt} = 4\pi r_p D_k \beta(r_p) \left(\frac{P_k - P_k^{\text{sat}}}{k_B T}\right) \times \theta \tag{4}$$

where $N_{k,p}$ is the number of molecules of type k on a particle of type p, D_k is the gas diffusivity in m^2/s, and P_k and P_k^{sat} are the partial and saturation pressures of species k, respectively, expressed in Pa. The function β accounts for changes in uptake in different gas regimes, and is described in equation A5. Experimentally-derived deposition coefficients for heteromolecular condensation, used in the calculation of β, are taken from Kärcher (1998). On soot particles, θ describes the fractional surface coverage of the particle liquid coating and is calculated according to Kärcher (1998). For all other particles, this limitation is ignored and θ is set to 1. Gas diffusivities for H_2SO_4 and HNO_3 are taken from Tang et al. (2014).

In addition to growth of existing particles, new liquid particles can form through binary homogeneous and heterogeneous nucleation. Several nucleation parameterizations have been established to simulate binary homogeneous nucleation in a sulfur-rich environment (Jaecker-Voirol and Mirabel, 1989; Napari et al., 2002; Vehkamäki et al., 2002). Jung et al. (2008) has computed different sensitivities using these models and provided further validation of the models cited previously, comparing the results to field measurements. Given the range of ambient conditions relevant to an aircraft plume, we calculate cluster size, composition, and nucleation rate using the parameterization from Vehkamäki et al. (2002). While this model is only considered valid between 230.15 K and 305.15 K, we expect that most nucleation of fresh sulfate aerosol will occur while the plume is still cooling down, within this temperature range. Liquid aerosols are assumed to remain liquid throughout the plume lifetime. Previous studies (e.g. Kärcher, 1998; Tabazadeh et al., 1997) have quantified the freezing behavior of sulfate aerosols and liquid sulfur soot coating at low temperatures and found that freezing of sulfate aerosols requires an ice supersaturation of about 1.5 at 210 K. Additionally, Kärcher et al. (1998) conclude that heterogeneous freezing on coated soot particles drives the contrail formation phase. We thus neglect the freezing of sulfate aerosols similarly to Wong and Miake-Lye (2010).

The number concentration of aerosol particles in the plume can also change through coagulation, as emitted and entrained particles collide and coalesce. During the early plume phase, we consider only the coagulation of liquid aerosols, and the scavenging of liquid aerosols by ice and soot particles. Self-aggregation of ice and soot particles on the time scale of the early plume is assumed to be negligible. Since all aerosols during this phase are likely to be small, all collisions are assumed to result in coagulation (a coalescence efficiency of 1) (Jacobson, 2011). Particle breakup and shattering is neglected for the same reason (Beard and Ochs III, 1995; Jacobson, 2011). The effect of coagulation on the number concentration of aerosols in size bin k, covering the size interval $[r_k, r_{k+1}]$, is modeled as

$$\frac{dn_k}{dt} = \frac{1}{2}\sum_{j=1}^{k-1} \text{K}_{j,k-j} n_j n_{k-j} - \sum_{j=1}^{+\infty} \text{K}_{k,j} n_k n_j, \tag{5}$$

where n_k is the number density of particles in bin k and $\text{K}_{i,j}$ is the coagulation kernel appropriate to collisions between size bins i and j, which represents the physics of the problem. A full description of the coagulation kernel and its calculation is given in Appendix B. Equation (5) states that the rate of change in the number density in bin k corresponds to the rate at which

https://doi.org/10.5194/acp-2019-498
Preprint. Discussion started: 17 July 2019

Atmospheric Chemistry and Physics Discussions

smaller particles of size $k-j$ coagulate with particles of size j minus the rate at which the particles of size k are lost due to coagulation with particle of all sizes.

During the early plume phase, liquid aerosols are modeled using 64 size bins, from a minimum radius of 0.1 nm to a maximum of 0.5 µm. Ice and soot aerosols are considered to have a single size, as estimated based on equations (3) and (4). Instead of solving equation (5) directly for every size bin, aerosol coagulation is computed using a semi-implicit, non-iterative, volume-conserving and unconditionally stable numerical scheme described in Jacobson et al. (1994). This model has been used extensively in aerosol modeling and aircraft plume simulations (Paoli et al., 2008). The rate of particle coagulation peaks shortly after emission and then significantly reduces as entrainment of ambient air into the plume decreases the number of aerosol particles present per unit volume of air.

The number and size of aerosols present at the end of the early phase is used to provide the initial conditions for the mature plume phase, with one adjustment. The downward movement induced by the aircraft wake vortices (Unterstrasser et al., 2008) increases the depth of the contrail, while adiabatic heating and turbulent temperature fluctuations result in crystal losses through sublimation. These losses are represented using a survival fraction, which we compute using a parameterization based on large-eddy simulations (Unterstrasser, 2016). This survival fraction is typically of the order of 0.5, such that the initial aerosol population for the mature plume phase includes roughly half the number of aerosol particles as were present at the end of the early phase.

2.3 Modeling of the mature plume

Following breakdown of the wingtip vortices, the plume is considered to enter the "diffusion regime". In this regime, the plume is no longer considered to be well mixed, and diffusion of chemical constituents becomes important.

In APCEMM, we use an operator splitting method which allows us to treat the chemical kinetics terms separately from the turbulent diffusion terms, and to apply optimized solution methods for these different processes. This includes in the representation of the domain. For chemistry calculations, the domain is represented using a set of fixed concentric elliptical rings (Figure 1). The central ring (semi-major and semi-minor axis of ~75 m and ~30m respectively) is initialized using chemical concentrations and aerosol properties as calculated at the end of the "early plume" stage, and after accounting for losses due to vortex sinking. All other rings are initialized with ambient air. Each ring is further discretized into a lower and upper half-ring to allow for vertical variations in temperature, and to account for sedimentation of aerosols.

Diffusion and advection of pollutants relative to the plume centerline (due to wind shear), in addition to sedimentation of aerosols and buoyant motion, are simulated on a regular, rectilinear grid with a horizontal and vertical grid spacing of ~100 m horizontally and ~5 m vertically. Prior to these "transport" processes, concentrations of constituents in the rings are mapped to the rectilinear grid. Diffusion, advection, and settling of the constituents is then simulated using a spectral scheme (Gottlieb and Orszag, 1977). This scheme is also used to allow shear to distort the chemical rings. Following transport, the constituents are mapped back to the ring discretization.

Diffusion of pollutants, chemistry, and aerosol microphysics are all explicitly accounted for using a time stepping scheme. All processes are simulated using a variable timestep. During the first 10 minutes, and within 10 minutes of local sunrise or sunset, the time step is restricted to 30 seconds to ensure that rapid chemical changes are captured. At all other times, a time step of 5 minutes is used.

2.3.1 Diffusion and shear in the mature plume

The rate of diffusion of the plume's constituents is modeled using directional diffusion coefficients. The degree of diffusion anisotropy is dictated by the Richardson number, a measure of local atmospheric stability (Dürbeck and Gerz, 1996; Schumann et al., 1998). In APCEMM, the horizontal and vertical diffusion coefficients D_h and D_v are calculated based on meteorological data, which must be supplied as part of the model input. D_v is estimated using the approach from Schumann et al. (1995) using the local Brunt-Väisälä frequency and Richardson number (a measure of local atmospheric stability), which is in turn computed from the local wind shear. To account for initial turbulence, D_v is increased to 1.1 m^2/s, after which it is reduced exponentially to its background value with an e-folding time of 13 minutes (Kraabøl et al., 2000). The horizontal diffusion coefficient is provided by the user, with a default value of 20 m^2/s. These values are consistent with literature estimates. Dürbeck and Gerz (1996) found that, for Richardson numbers above unity, the horizontal and vertical diffusion coefficients lie in the range $15\ m^2/s \leq D_h \leq 23\ m^2/s$ and $0.15\ m^2/s \leq D_v \leq 0.18\ m^2/s$ respectively, which agree with measurements from Schumann et al. (1995).

In addition to diffusion across the domain, advection of air due to wind shear is explicitly accounted for using the same spectral scheme as is applied to simulate diffusion. The horizontal wind speed relative to the plume center line is calculated assuming a constant vertical wind shear across the domain.

https://doi.org/10.5194/acp-2019-498
Preprint. Discussion started: 17 July 2019

Atmospheric Chemistry and Physics Discussions

We also simulate bulk vertical motions of the air mass. Heymsfield et al. (1998) reported through *in situ* measurements the existence of large-scale vertical motion in an aircraft wake. This upward motion is predominantly due to absorption of upwelling infrared radiation, resulting in a radiative imbalance (Jensen et al., 1998). The contrail net heating drives a local updraft with speeds of up to 10 cm s^{-1} during the first hour (Heymsfield et al., 1998), consistent with estimates that the contrail core can rise over the first hour after its formation (Jensen et al., 1998). To account for such large-scale vertical motions of the plume, we simulate the plume as remaining stationary but move the temperature field vertically according to the updraft velocity. We adopt an exponentially-decaying velocity profile with a time scale of one hour.

2.3.2 Chemistry in the mature plume

The gas-phase chemistry mechanism is taken from GEOS-Chem v11 (Eastham et al., 2014). Heterogeneous halogen, N_2O_5 and HO_x chemistry, as well as formation and evaporation of stratospheric aerosols are considered. Due to their long lifetimes, reactions involving CFCs and HCFCs are neglected. The set of chemical reactions is solved numerically with KPP (Damian et al., 2002).

2.3.3 Aerosol modelling in the mature plume

As the plume expands, the ice crystal size distribution changes due to growth, evaporation, gravitational settling and coagulation. Particle growth is treated using a moving-center size structure (Jacobson, 1997). Ice crystal growth is characterized by the "advection" of the particle density distribution across diameter space (Jacobson, 2003).

Ice crystal growth modifies the particle volume but leaves the number of particles constant. Sublimation mechanisms lead to a loss of ice crystals and act as a source of water vapor, modifying the cell's relative humidity and release a dry particle core which is then considered "deactivated" and unable to take up water vapor as ice. The extent of sublimation is moderated by the size of the droplet cores, as larger hydrometeors can persist in subsaturated air. Evaporation and sublimation are both endothermic processes that cool down the surface of an ice crystal. The equilibrium surface temperature is obtained through an iterative process that allows us to compute the particle sublimation rate (Jacobson, 2003).

Aggregation of ice particles uses the same algorithm and the same coagulation kernel described previously for sulfate aerosols. Ice particles can reach sizes of the order of 10 µm indicating that particle collisions do not necessarily lead to coagulation and that bounce-off can occur. The coalescence efficiency is computed from the work of Beard and Ochs III (1995) by the following Newton-Raphson algorithm (valid for particles smaller than 300 µm):

$$E_{n+1} = E_n - \ldots \frac{A_0 + A_1 E_n + A_2 E_n^2 + A_3 E_n^3 - \ln(r_s) - \ln(r_b/200)}{A_1 + 2A_2 E_n + 3A_3 E_n^2}, \quad (6)$$

where n is the iteration step, E_n the coalescence efficiency at iteration n, and r_s and r_b the small and big particle radii respectively, expressed in micrometers. The constants $A_0 = 5.07$, $A_1 = -5.94$, $A_2 = 7.27$ and $A_3 = -5.29$ are taken from Beard and Ochs III (1995). This algorithm is described in more detail in Jacobson (2011). We use 85 size bins for ice particles, covering radii from 50 nm to 100 µm.

Gravitational settling causes the ice particles to fall vertically, thus entering warmer regions. Ice particle terminal velocities are computed according to Stokes law, accounting for the slip correction, as in Pruppacher et al. (1998). The settling velocity of an ice crystal depends on its size, with larger particles falling faster. Different parts of a contrail have different crystal sizes, meaning that they settle at different speeds (Unterstrasser et al., 2016). This differential settling effect is often neglected in reduced-order contrail models.

Finally, liquid (sulfate) aerosols are modeled using the same 64-bin approach as in the early plume phase. In the mature plume phase, the distribution of sulfate aerosols is affected only by coagulation, using the same coagulation kernel as before.

2.4 Experimental description

We first simulate the chemical evolution of a plume from a single flight using both approaches and compare the results to the literature (section 3.1). We then compute the impact of changes in background conditions (section 3.2, engine emissions (section 3.3), and flight location (section 3.4). These simulations are intended to both validate the ability of APCEMM to accurately model non-linear plume chemistry and to quantify the extent to which the output of an instant dilution approach differs from that of a fully resolved plume model,

We also perform a set of dedicated experiments to quantify the relationship between different parameters and the behavior of a contrail forming in the plume. This includes the role of relative humidity and updraft velocity (section 3.5.1), and the effect of

https://doi.org/10.5194/acp-2019-498
Preprint. Discussion started: 17 July 2019

Atmospheric Chemistry and Physics Discussions

changes in soot emissions (section 3.5.2). Finally, we combine these assessments to determine how accounting for contrail ice could directly affect the chemistry of the plume, and how this effect is modified by changes in soot emissions (section 3.5.3). Most global models do not include contrail simulation, so only APCEMM results are provided in these sections.

All plumes are simulated for 24 hours. For typical diffusion parameters of D_h = 15 m^2/s and D_v = 0.15 m^2/s, this results in 0.03% of emitted material reaching the edge of the computational domain by the end of the simulation.

2.4.1 Model setup

Both models, APCEMM and the instant-dilution approach, are initialized with background mixing ratios obtained from a year-long GEOS-Chem simulation. Noontime photolysis rates are retrieved from that same run. Atmospheric background conditions are obtained from a spin-up run over 5 days. Meteorological data for each altitude, latitude, longitude, and time are taken from the Modern-Era Retrospective analysis for Research and Applications, Version 2 (MERRA-2) for 2013. This includes the vertical wind shear and (longitudinally-averaged) Brunt-Väisälä frequency, used for calculation of the vertical diffusion coefficient. This approach provides an upper bound on vertical diffusion, as it overpredicts the diffusion parameter at large Richardson numbers. The probability distribution of the Brunt-Väisälä frequency, Richardson number, and resulting vertical diffusion parameter are given in the SI for different pressure levels. As shown in Dürbeck and Gerz (1996), the Brunt-Väisälä distribution is unimodal in the troposphere and peaks around $N = 0.01\ s^{-1}$. A second mode appears in the stratosphere at approximately $N = 0.02\ s^{-1}$. Some further analysis shows that 90% of the distribution lies at Richardson numbers greater than 5, indicating weak and/or fast decaying turbulence. The distribution and its support agree with the values in Schumann et al. (1995) and the mean values lie in the range given by Dürbeck and Gerz (1996). A horizontal diffusion parameter D_h of 20 m^2/s is assumed for all simulations. Unless otherwise specified, we assume zero wind shear, although the effects of this assumption are investigated.

All the cases in this analysis consider emissions from a B747-8 equipped with GEnx engines, which are released in the innermost ring, which has a cross-sectional area of 6,000 m^2.

2.4.2 Metrics of the chemical response

To evaluate the error resulting from neglecting non-linear plume chemistry, we compare results generated using the instant dilution approach and using APCEMM. The discrepancies between both models are first compared in terms of total ozone mass per unit length in flight direction (kg/km). In addition, the conversion of short-lived nitrogen oxides to reservoir species affects long-term ozone production, heterogeneous chemistry, particle formation and/or growth, with known long-term impacts on air quality (Eastham and Barrett, 2016). The evolution of nitrogen partitioning is therefore computed for both models.

The total emitted NO_y (E_{NO_y}) is a conserved quantity throughout the plume lifetime and is equal to the plume-integrated NO_y perturbation $\left(E_{NO_y} = \Delta\left(NO_y\right) = \iint_A \left(\left[NO_y\right] - \left[NO_y\right]^{Amb}\right) dA\right)$, where the notation $[\cdot]^{Amb}$ refers to ambient conditions. At any given instant $\Delta\left(NO_y\right)(t) = \Delta\left(NO_x\right)(t = 0)$, which is proportional to the NO_x emission index. Averaging the perturbation due to aircraft emissions allows us to compute the time-dependent chemical conversions from one species to another. The emission conversion factor of species X, ECF_X, is then defined as:

$$ECF_X(t) = \frac{1}{E_{NO_y}} \iint_A \left([X](t) - [X]^{Amb}(t)\right) dA. \tag{7}$$

The emission conversion factor quantifies how many moles of species X are obtained for one mole of emitted NO_y. For ozone, this is similar to the ozone production efficiency (OPE), although the ECF is time-dependent and does not include ozone which has been produced and later destroyed. Given that nitrogen oxides are converted to reservoir species over the plume lifetime, ECF_{NO_x} decreases with time.

We use the ECF to quantify the discrepancy between the two approaches. For a species X, we define the error as the difference in ECF after 24 hours:

$$\varepsilon_X = ECF_X^{Box}(t = 24\ \text{hrs}) - ECF_X^{APCEMM}(t = 24\ \text{hrs}). \tag{8}$$

Evaluation after 24 hours ensures that the domain is in the same photochemical state as at initialization. A positive error means that instant dilution of aircraft emissions overestimates the chemical production of species X compared to the aircraft plume model.

https://doi.org/10.5194/acp-2019-498
Preprint. Discussion started: 17 July 2019

Atmospheric Chemistry and Physics Discussions

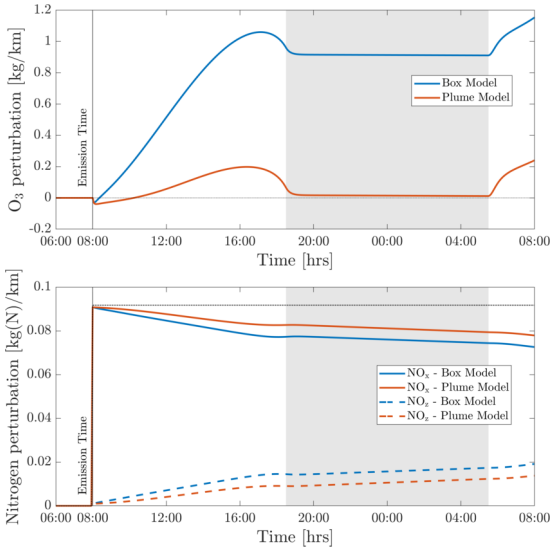

Figure 2. Perturbations in ozone (O_3), nitrogen oxides (NO_x) and the nitrogen reservoir species (NO_z) according to simulations using an instant dilution approach and the plume model. Emissions are released at 8:00 AM local time in a polluted environment. The black dotted line represents all nitrogen species (NO_y), which is a conserved quantity. The shaded areas correspond to nighttime.

3 Results

3.1 Limitations of instant dilution

We first simulate the evolution of an aircraft plume as simulated using APCEMM. Figure 2 shows the time series of the ozone and NO_x perturbations over the first 24 hours after emission. The results as calculated under an instant dilution assumption (single, well-mixed box) are also shown.

The chemical evolution of the plume can be split into three regimes, distinct from the dynamical regimes described in section 2.1 (Song et al., 2003; Vinken et al., 2011). The first regime is characterized by very high NO_x mixing ratios (>1 ppmv), causing ozone titration. In this period, typically lasting 10 minutes, high mixing ratios of nitric oxide (NO) rapidly deplete local ozone concentrations, resulting in a burst of NO_2 production through reaction [A1] (see Table 3). In this regime, HO_x ($= OH + HO_2$) production is suppressed by the lack of ozone (reactions [A5-A6]).

As the plume dilutes and NO_x mixing ratios fall below 1 ppmv, it enters the second regime. With little ozone remaining, HO_2 reacts with the remaining NO (reaction [A4]), producing OH and NO_2 without depleting ozone. This leads to increased OH levels and enhanced ozone production. Meanwhile, photolysis of NO_2 through reaction [A2] results in the recovery of ozone which had been depleted during the first regime. Between one and two hours after emission, ozone has been restored to its background value. Reactions [A7] through [A10] lead to conversion of emitted NO_x to nitrogen reservoir species.

A few hours after emission, the third regime begins, characterized by NO_x mixing ratios below 1 ppbv. Reaction [A4] and reactions including organic peroxides (such as [A12]) cause increasing levels of ozone and additional conversion to reservoir species. Aircraft plumes, similarly to ship plumes, are characterized by a high NO_x to volatile organic compound (VOC) ratio, therefore favoring termination reactions (e.g. [A7]) over catalytic ozone formation (Song et al., 2003).

Differences between the model outputs are dominated by the behavior during the first two regimes. Explicitly modeling the plume allows the initial ozone destruction to be captured because the highly-concentrated plume is resolved. Although a recovery in ozone is later simulated once the plume diffuses, additional production which would have occurred during the early plume is prevented.

In the instant dilution model, this ozone destruction and production cut-off is not captured. Because ozone is not locally depleted, the instant dilution model instead simulates a prolonged period of net ozone production, as HO_x concentrations remain close to background values. The instant dilution approach, unlike APCEMM, bypasses the first two HO_x-limited regimes and is therefore in a NO_x-rich, HO_x-rich environment, favoring daytime ozone production and conversion of NO_x to reservoir species. Additionally, instant dilution of aircraft emissions results in shorter NO_x lifetimes (see Appendix C for more details).

https://doi.org/10.5194/acp-2019-498
Preprint. Discussion started: 17 July 2019

Atmospheric Chemistry and Physics Discussions

Table 3. Dominant $O_3/NO_y/HO_x$ reaction pathways in APCEMM.

Reaction #	Reaction
[A1]	$NO + O_3 \longrightarrow NO_2 + O_2$
[A2]	$NO_2 + h\nu \longrightarrow O(^3P) + NO$
[A3]	$O(^3P) + O_2 \longrightarrow O_3$
[A4]	$NO + HO_2 \longrightarrow NO_2 + OH$
[A5]	$O_3 + h\nu \longrightarrow O(^1D) + O_2$
[A6]	$O(^1D) + H_2O \longrightarrow 2OH$
[A7]	$NO_2 + OH + M \longrightarrow HNO_3 + M$
[A8]	$NO_2 + O_3 \longrightarrow NO_3 + O_2$
[A9]	$NO_3 + NO_2 \longrightarrow N_2O_5$
[A10]	$N_2O_5 + H_2O \xrightarrow{\text{Aerosol}} 2HNO_3$
[A11]	$CH_4 + OH \longrightarrow CH_3O_2 + H_2O$
[A12]	$CH_3O_2 + NO \longrightarrow HCHO + \ldots$ $HO_2 + NO_2$
[A13]	$CO + OH \longrightarrow CO_2 + H$
[A14]	$H + O_2 + M \longrightarrow HO_2 + M$
[A15]	$RH + OH \xrightarrow{O_2} RO_2 + H_2O$
[A16]	$RO2 + NO \longrightarrow RO + NO_2$

R represents an organic compound. The RH notation is used to describe Volatile Organic Compounds (VOCs).

The net result is that, after 24 hours, the instant dilution approach estimates that the aircraft plume has produced ~1.2 kg of ozone per kilometer flown, compared to ~0.2 kg per kilometer estimated by APCEMM. By this stage in the simulation both models show similar chemical behavior, as the plume has become sufficiently dilute to be well-represented by the instant dilution model. However, the erroneous simulation of ozone production in the initial phase leads to a persistent and significant error in the net ozone production of the plume.

This behavior, and the discrepancy between APCEMM and an instant dilution model, is strongly affected by local meteorology. Increased diffusion, or equivalently higher wind shear, dilutes the plume with a larger mass of air, minimizing ozone depletion. Therefore, total ozone production scales directly with mixing parameters. Table 4 shows the remaining NO_x and total mass of produced ozone after 24 hours as a function of the local diffusion coefficients. The results for instant dilution are shown in the last row. As diffusion rates increase and dilution becomes faster, the discrepancy between APCEMM and the instant dilution model decreases towards zero. Errors in global simulation of aircraft impacts will therefore be maximized in regions with low diffusion and/or wind shear.

3.2 Influence of background conditions

The in-plume ozone perturbation ($\Delta[O_3](t)$) and the conversion efficiency of NO_x to NO_y are influenced by parameters such as the emission time and background conditions. We first investigate the influence of changes in background NO_x. Figure 3 shows how the 24-hour ozone emission conversion factor, ECF_{O_3}, varies as a function of NO_x background concentration and date of emission. Both simulations have been integrated over 24 hours. All simulations are conducted after a 5-day spin-up, and are simulated as occurring at 220 hPa altitude and 60° N.

The results agree qualitatively with the simulations from Petry et al. (1998). The instant dilution approach overestimates ozone production for any emission time, with emission conversion factors up to three times their respective values for the plume model. For any given background NO_x concentration, discrepancies between the two models are greatest during summertime. However, as background NO_x is increased, the overall ozone perturbation due to the aircraft plume decreases in both models. Doubling the background NO_x mixing ratio from 100 to 200 pptv results in a relative reduction of the ozone perturbation by 30 to 45% during summertime. During wintertime, the net effect of NO_x emissions is to instead decrease ozone. This pattern is explained by a less efficient conversion of NO_x to reservoir species at night. The transition between net positive and net negative ozone also changes as a function of the background NO_x. At 50 pptv of background NO_x, the plume model simulates net ozone

https://doi.org/10.5194/acp-2019-498
Preprint. Discussion started: 17 July 2019

Atmospheric Chemistry and Physics Discussions

Table 4. Influence of diffusion parameters and wind shear on in-plume chemistry

	Diffusion coefficients $[m^2/s]$	Remain. NO_x [%]	O_3 perturbation [kg/km]
$s = 0.000\ s^{-1}$	$D_h = 05, D_v = 0.05$	88.2	0.0633
	$D_h = 10, D_v = 0.10$	86.2	0.170
	$D_h = 15, D_v = 0.15$	84.9	0.262
	$D_h = 20, D_v = 0.20$	84.0	0.340
	$D_h = 25, D_v = 0.25$	83.4	0.408
$s = 0.003\ s^{-1}$	$D_h = 05, D_v = 0.05$	86.2	0.0780
	$D_h = 10, D_v = 0.10$	84.4	0.207
	$D_h = 15, D_v = 0.15$	83.6	0.310
	$D_h = 20, D_v = 0.20$	82.6	0.422
	$D_h = 25, D_v = 0.25$	82.1	0.470
	Instant dilution:	79.12	1.2581

Data obtained 24 hours after emission.

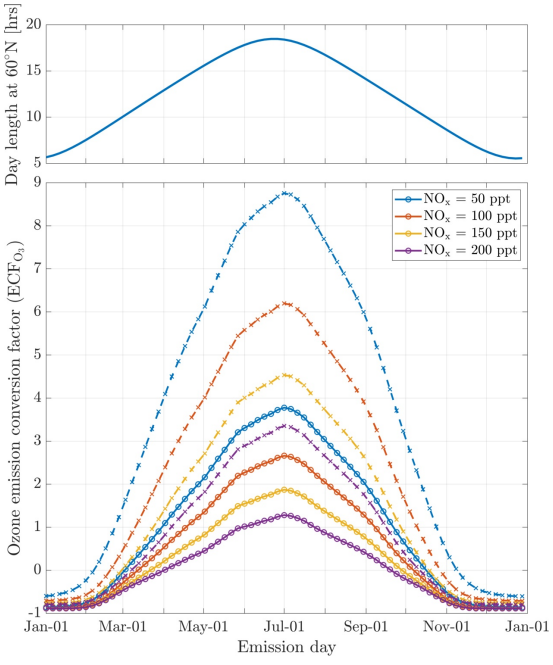

Figure 3. The bottom figure displays the 24-hour ozone emission conversion factor from the emission of a B747-8 equipped with GEnx engines at 08:00 local time, at 60° N, for a single box model (dotted lines) and the plume model (continuous lines) as a function of day of the year. Different scenarios representing different background NO_x mixing ratios are displayed. The cases correspond to a background O_3 mixing ratio of 52 ppb. The figure on the top displays the amount of sunlight received at 60° N throughout the year, expressed in hours of daytime.

production for 10 months, compared to 8 months in the instant dilution model. At 200 pptv, net production is simulated for 6 and 5 months by the two models respectively. This inconsistency in the magnitude and sign of the error between the two models means that the true impact of aviation emissions will be inconsistently modeled by an instant dilution approach.

At a finer scale, we observe variations in emissions impacts depending on the time of day of the emission. Figure 4 shows contours of ozone and NO_x emission conversion factors for different times of day over the course of a year. For most of the year, the total production of ozone is relatively insensitive to the exact time of day of the emission. The exception is during

https://doi.org/10.5194/acp-2019-498
Preprint. Discussion started: 17 July 2019

Atmospheric Chemistry and Physics Discussions

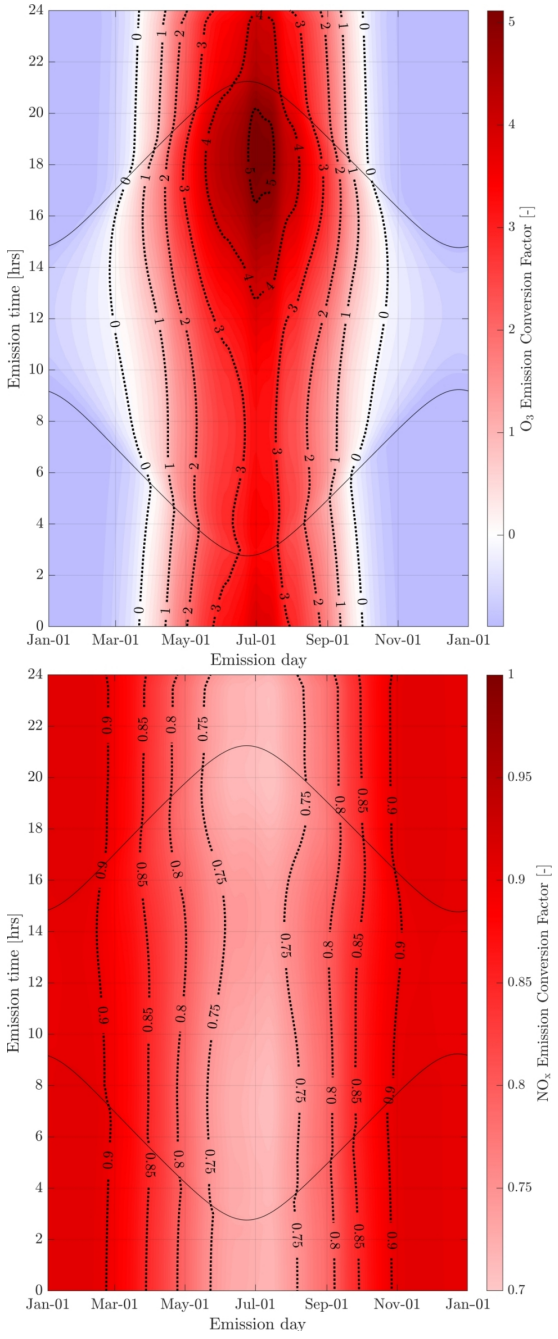

Figure 4. 24-hour O_3 (top) and NO_x (bottom) emission conversion factors from the emission of a B747-8 equipped with GEnx engines at 60° N. Dotted lines represent sunrise and sunset at the given latitude.

local summertime, when emissions immediately before local sunset (the upper dotted line) cause almost twice as much ozone to be produced as an emission during late morning. This is discussed in more detail in Appendix C.

https://doi.org/10.5194/acp-2019-498
Preprint. Discussion started: 17 July 2019

Atmospheric Chemistry and Physics Discussions

Table 5. Influence of NO_x emission index on emission conversion factors and in-plume ozone perturbation

EI_{NO_x} [g/kg_{fuel}]	ECF_{O_3} [-]	ECF_{NO_x} [-]	$\Delta[O_3]$ (24 h) [pptv]
EI_{NO_x} = 8.0	3.24	0.772	59.33
EI_{NO_x} = 12.0	2.43	0.790	66.74
EI_{NO_x} = 16.0	1.91	0.805	69.79
EI_{NO_x} = 20.0	1.54	0.818	70.49

Data obtained 24 hours after emission and for emission at 8:00 on June 16th.

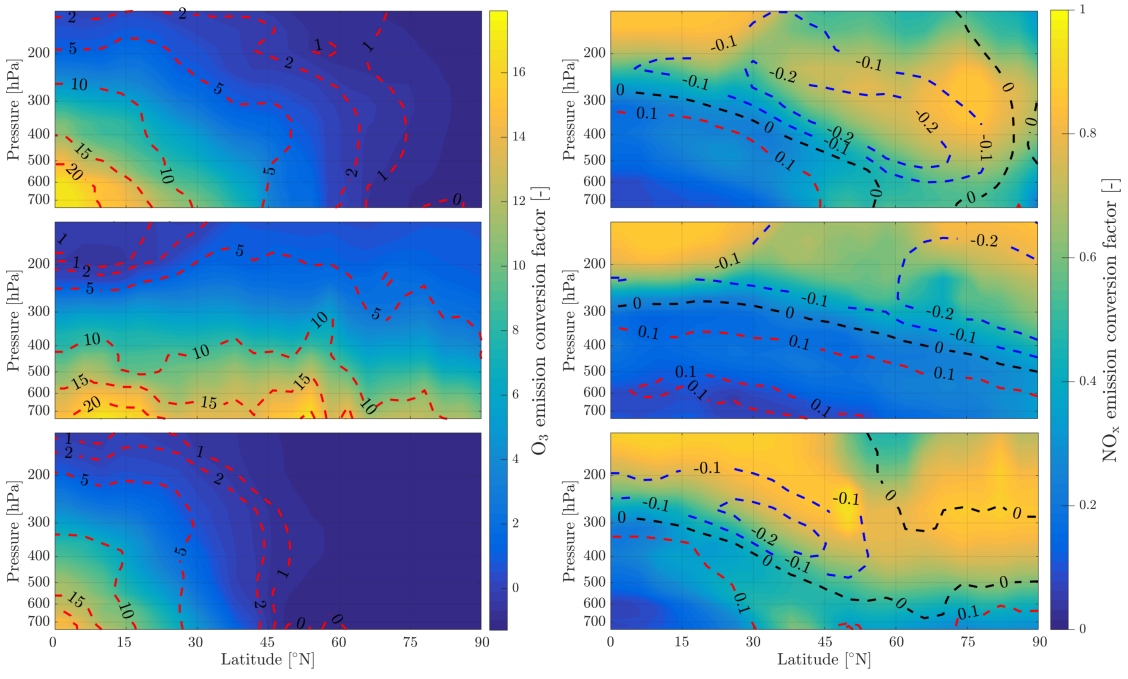

Figure 5. Contour plots of O_3 (left) and NO_x (right) conversion emission factor, 24 hours after emission from APCEMM. The isolines represent the discrepancy between the instant dilution approach and APCEMM. Blue isolines represent cases where the species ECF is underestimated, whereas the red isolines signify that the quantity is overestimated by instant dilution. Simulations have been carried out for emissions at 8:00 on March 21st, June 21st and December 21st (from top to bottom).

3.3 Influence of NO_x emissions index

The total NO_x emitted into the plume also affects chemical outcomes. Table 5 shows how a range of impact metrics are affected by changes in the NO_x emissions index. The overall ozone ECF decreases as the NO_x emissions index increases, falling from 3.24 for an EI of 8 g/kg fuel to 1.54 for an EI of 20 g/kg. However, the product of these two factors - proportional to the total ozone present after 24 hours - still increase monotonically with the emissions index of NO_x over the range of values considered.

This implies that decreasing the NO_x emissions index provides non-linear benefits in terms of total ozone production. A one unit increase in the NO_x emission index (expressed in g/kg_{fuel}) leads to a reduction in ECF_{O_3} of 0.08 mol/mol under high EI_{NO_x} scenarios, but this increases to 0.2 mol/mol for the same absolute reduction in the NO_x under low EI_{NO_x} scenarios.

These results agree with the findings from Petry et al. (1998), Meijer (2001) and Vohralik et al. (2008). These simulations suggest that, relative to a plume-scale treatment of chemical processes, conventional instant-dilution approaches overestimate ozone production by up to a factor of three, and overestimate conversion of nitrogen oxides to reservoir species. We also find that decreasing aircraft emissions of NO_x emissions yields accelerating returns in terms of total in-plume ozone production, but that these results are sensitive to background NO_x concentrations.

https://doi.org/10.5194/acp-2019-498
Preprint. Discussion started: 17 July 2019

Atmospheric Chemistry and Physics Discussions

Table 6. Discrepancies between the box model and APCEMM at cruise altitudes. The left-most column shows the average ozone ECF as calculated in APCEMM, while the central column shows the average discrepancy in ECF between the instant dilution model and APCEMM. The right-most column shows the maximum calculated error. A positive error value means that the instant dilution model overestimates ozone production. All variables are evaluated and averaged over cruise altitudes only.

Date	$\overline{\mathrm{ECF}_{\mathrm{O_3}}}$	$\overline{\varepsilon_{\mathrm{O_3}}}$	$\max(\varepsilon_{\mathrm{O_3}})$
03/21	+0.185	+2.566	+5.535
06/21	+0.977	+2.371	+4.445
12/21	-0.306	+1.951	+5.310

3.4 Influence of pressure and latitude

The atmospheric response to aircraft emissions also varies as a function of the pressure and latitude of the emission. Although latitude is not a physical parameter of the model, it is equivalent to defining the amount of sunlight received, which affects photolysis rates and background conditions. We simulate pressures from 750 hPa to 150 hPa and latitudes from 0°N to 90°N. Temperature data is taken from monthly-averaged MERRA-2 meteorological data, for 2013. To capture variation of a single flight's emission conversion factors with geographic location and altitude, background conditions and photolysis rates are taken from GEOS-Chem. To also capture seasonal effects, simulations are carried out for emissions taking place on the winter and summer solstices as well as during the spring equinox, on March 21st. Simulations using both models are performed. Results are presented in Figure 5 in terms of ozone and NO_x emission conversion factors. Isolines of the discrepancy between both models are plotted on Figure 5 for O_3 and NO_x (ε_{O_3} and ε_{NO_x}).

The results show a link between ozone production efficiency and latitude and pressure as previously observed by Vohralik et al. (2008). Increasing pressure enhances the ozone emission conversion for the same amount of emitted NO_x, given sufficient sunlight. The amount of sunlight drives ozone production, as little ozone is generated in the most northern latitudes during winter. At high flight altitudes or in cold regions, the daytime NO_x-driven ozone production is of the order of magnitude of the ozone loss at dusk and the early titration effect. This cancellation leads to a small in-plume ozone perturbation of varying sign as shown previously (Vohralik et al., 2008).

The instant dilution approach consistently overestimates the amount of ozone produced at cruise altitudes (~150 to ~240 hPa), as shown in Table 6. In absolute terms, the box model performs worst during summertime when ozone production is enhanced across the Northern hemisphere and the discrepancy in the ozone emission conversion factor (ε_{O_3}) is larger. The maximum ozone discrepancy (Table 6) reaches values around 5 in all seasons, corresponding to a relative error of approximately +200%.

NO_x conversion shows different sensitivities to location than the ozone ECF. As shown in the right panels of Figure 5, the NO_x ECF is positively correlated with ambient temperature but is insensitive to the amount of sunlight and season. As the temperature decreases with increasing altitude in the troposphere, the conversion of NO_x to NO_y is lowest at high altitude, going from an average value of 0.3 at 700 hPa to approximately 0.75 at 150 hPa. Greater conversion occurs in hotter air, around the equator and the tropics. Furthermore, the box model underestimates the amount of remaining NO_x at high altitudes (as seen in section 3.1) but overestimates at lower levels. The crossover point varies significantly with season and latitude.

3.5 Contrail microphysical, optical, and chemical properties

All analysis thus far has concerned conditions which are subsaturated with respect to ice. The simulated plumes have therefore been made up only of gas-phase constituents and non-ice aerosols. However, a second discrepancy between instant dilution models and real aircraft plumes is the lack of condensation trails in simulated aircraft exhaust, which can cause both climate and chemical impacts. This section assesses APCEMM's ability to simulate aircraft-induced condensation trails ("contrails"), quantifying how changes in background conditions affect the properties of the contrail. We then quantify the effect that these condensation trails have on the long-term atmospheric effects of aircraft emissions. This includes an investigation of differences in contrail lifetime and effects when forming in the stratosphere, as may result from supersonic flight.

3.5.1 Contrail simulations and the impact of relative humidity and initial updraft velocity

We first simulate the formation and evolution of a contrail in aircraft exhaust under a variety of conditions, to quantify the range of likely behaviors and verify behavior consistent with observations. For these purposes, we simulate an aircraft plume

https://doi.org/10.5194/acp-2019-498
Preprint. Discussion started: 17 July 2019

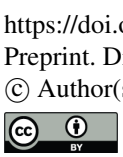

Atmospheric Chemistry and Physics Discussions

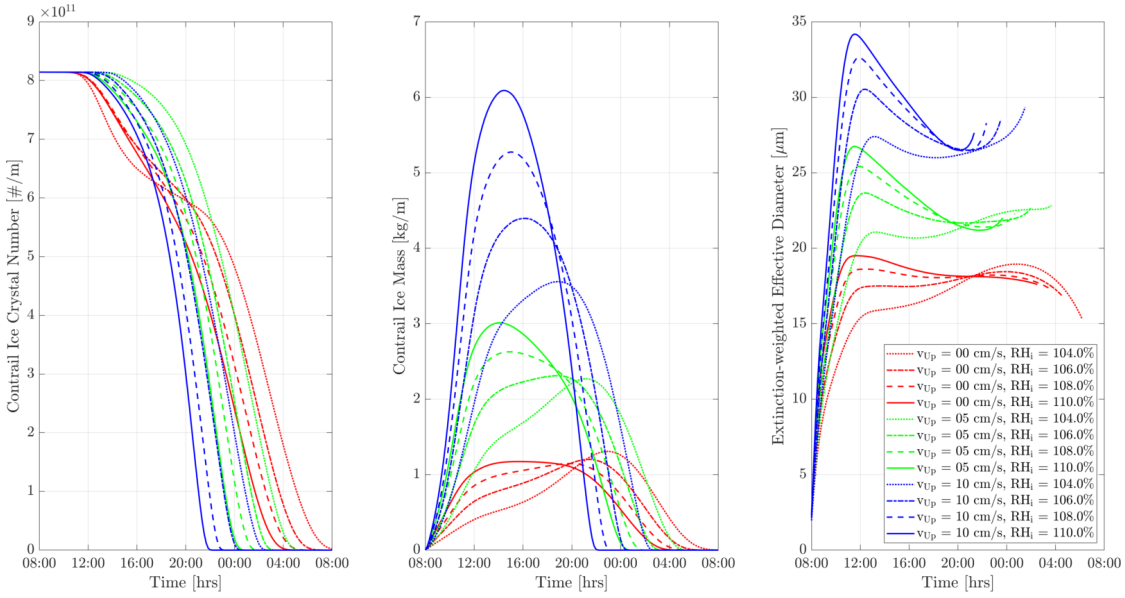

Figure 6. Contrail ice crystal number (left), ice crystal mass (middle) and extinction-weighted effective diameter (right) when varying background relative humidity and the updraft velocity magnitude.

in locally supersaturated air, with relative humidities from 102% to 108%. We also simulate a range of updraft velocities, from 0 to 10 cm/s. This is based on previous studies which have shown that heating of contrail ice induces an upward convection motion with velocities in this range, such that the plume enters a colder and moister environment (Unterstrasser and Gierens, 2010b; Unterstrasser et al., 2017). The depth of the moist layer is kept constant at 200 m for all simulations. Atmospheric shear is set to 0.004 s^{-1}. A diurnal temperature variation with a 0.1 K amplitude is applied, corresponding to daily temperature fluctuations in the upper-troposphere (Seidel et al., 2005).

Figure 6 shows the temporal evolution of total contrail ice crystal number and mass for each combination of parameters, as well as the extinction-weighted effective diameter (Unterstrasser and Gierens, 2010a). In all cases, the contrail persists for at least 14 hours, but has evaporated after 24 hours. These lifetimes are consistent with observations, in spite of the idealized meteorological conditions considered here (Minnis et al., 1998; Iwabuchi et al., 2012). Most ice crystals are lost through sublimation and *in situ* losses, represented in the coagulation kernel applied during the diffusion regime. *In situ* losses correspond to the sublimation of small crystals in favor of larger crystals when the relative humidity approaches 100%. This phenomenon is attributed to Ostwald ripening through the Kelvin effect (Lewellen et al., 2014; Unterstrasser et al., 2017). Losses through Brownian coagulation are negligible as they account for less than 1% of particle losses. As the contrail expands, the contrail core is dehydrated through gravitational sedimentation of the largest particles, leaving behind a population of smaller ice crystals with little ice mass but a significant surface area. The formation and settling of large ice crystals (with a radius greater than 30 μm) lead to early variations in contrail ice mass. This means that growth in contrail ice mass slows earlier than would be captured by reduced order models which consider only the mean settling velocity.

The contrail ice mass and the extinction-weighted effective diameter peak between 3 and 9 hours after formation, with variations in timing affected by both the updraft velocity and background relative humidity. In both cases, higher values result in greater overall water uptake and therefore larger ice particles. These larger particles then fall to warmer altitudes and melt, reducing the available number of particles. Higher relative humidity and updraft velocities also increase the extinction-weighted effective diameter for the same reason. This results in a tradeoff between the "size" of the contrail, in terms of either the ice mass or effective diameter, and its lifetime, with more massive contrails having shorter lifetimes. The sinusoidal pattern in contrail ice mass is caused by diurnal variations in temperature.

https://doi.org/10.5194/acp-2019-498
Preprint. Discussion started: 17 July 2019

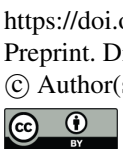

Atmospheric Chemistry and Physics Discussions

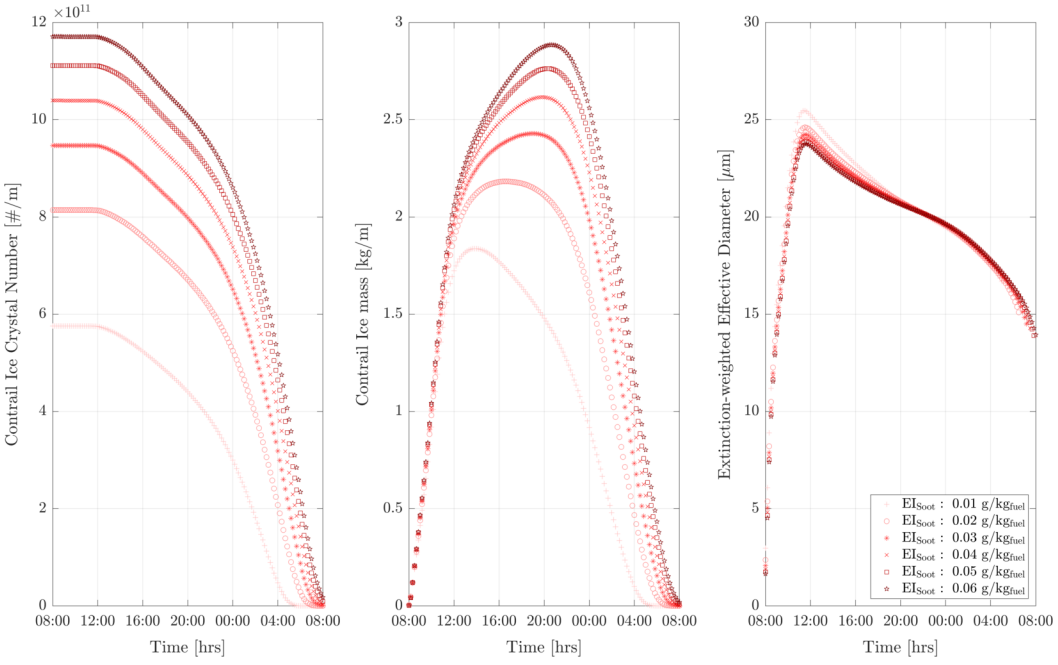

Figure 7. Total contrail ice crystal number (left), ice crystal mass (middle) and extinction-weighted effective diameter (right) for different soot emission indices.
A background relative humidity of 110%, a temperature of 210 K at flight level are assumed.

3.5.2 Influence of engine soot emission index on contrail properties

We next model how changes in soot emissions affect the properties of the contrail. We simulate an aircraft plume with soot emissions indices from 0.01 to 0.06 g/kg fuel. Each simulation assumes a uniform temperature of 210 K, a relative humidity of 110%, and a post-vortex sinking updraft of 5 cm s^{-1}.

Figure 7 shows the evolution of the total ice particle number, total ice mass, and extinction-weighted effective diameter for each emissions scenario. Considering first the total ice mass, two distinct regimes are visible. The first regime occurs over the first three hours after formation. In this regime, all cases have identical ice masses. The contrail ice mass is controlled only by the ambient relative humidity, as all available water mass is taken up by whatever particles are available, with lower emissions indices result in larger crystals.

After three hours, the simulations with the lowest emissions indices start to lose ice mass. This is because of the discrepancy in ice crystal radius. Since the same ice mass is taken up on a smaller number of particles, they become larger and fall more rapidly to warmer altitudes. Lower emissions indices result in smaller particles, extending the lifetime of the contrail. As the largest crystals are removed, only a core of small crystals remains.

These changes in contrail ice also affect the optical thickness of the plume. We calculate optical thickness by integrating the extinction χ, as defined in Ebert and Curry (1992). Figure 8 shows the temporal evolution of the optical thickness, integrated over the vertical and horizontal (perpendicular to the flight path) axes. As seen previously, the ice water content is identical in the first few hours for all simulations, meaning that a scenario with a large particle number has a larger total crystal surface area. This means that reducing the soot emissions index decreases both the optical depth of the contrail and its lifetime. This is quantified in table 7, which quantifies the "predominant" optical depth as

$$\tau_{\mathrm{pre}}(t) = \frac{\int \tau^2(x,t)dx}{\int \tau(x,t)dx} \tag{9}$$

https://doi.org/10.5194/acp-2019-498
Preprint. Discussion started: 17 July 2019

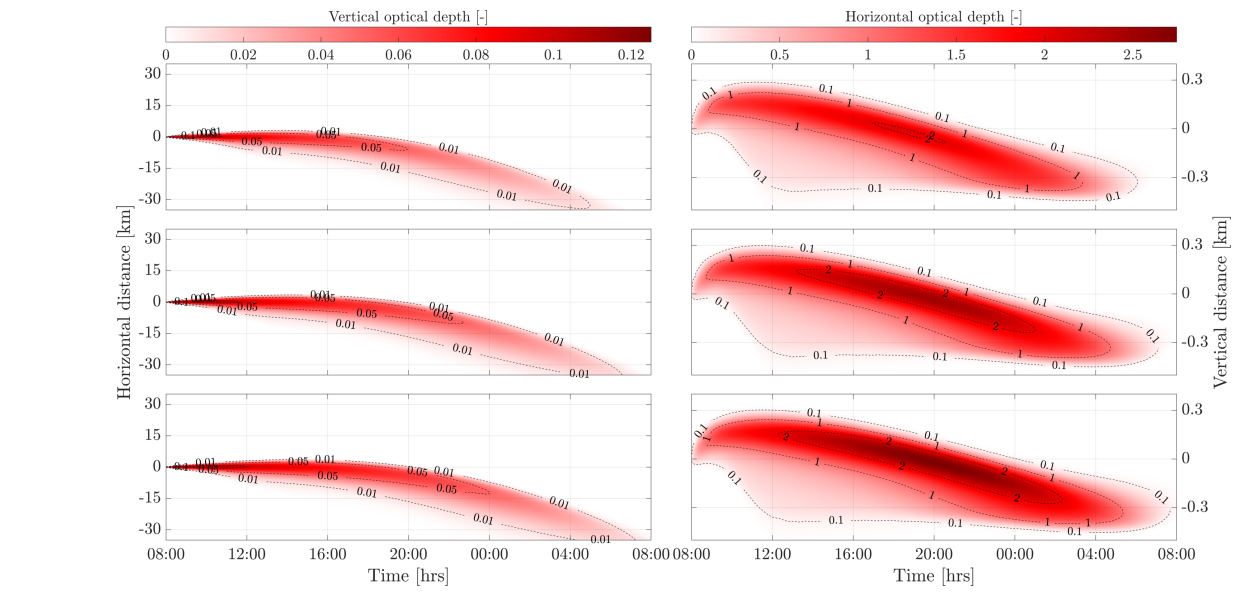

Figure 8. Contours of optical thickness along the vertical (left) and horizontal (right) direction for different soot emission indices: 0.02 (top), 0.04 (center), 0.06 g/kg$_{fuel}$ (bottom) respectively.
The horizontal axis is centered on the flight location. The vertical axis represents the distance with respect to the altitude after vortex sinking. The flight altitude before vortex sinking was at a pressure altitude of 10.6 km. Vortex sinking caused the plume to settle at a new altitude, 112 m lower, corresponding to the origin of the vertical axis. We apply a wind shear of 0.004 s^{-1}, causing the contrail to move left of the initial center line while sinking.
An optical depth of 0.1-0.2 is usually given as a contrail detection threshold through satellite sensing (Kärcher et al., 2009).

Table 7. Predominant optical depth for different soot emission scenarios

EI$_{BC}$ (g/kg$_{fuel}$)	10 min	1 hour	5 hours	10 hours
0.01	0.0645	0.0715	0.0491	0.0316
	-7.59%*	-10.7%*	-13.8%*	-23.1%*
0.02	0.0698	0.0801	0.0569	0.0411
	-	-	-	-
0.04	0.0716	0.0866	0.0629	0.0485
	+2.58%*	+8.11%*	+10.51%*	+18.0%*
0.06	0.0718	0.0900	0.0659	0.0524
	+2.86%*	+12.4%*	+15.8%*	+27.5%*

* Relative to a soot emission index of 0.02 g/kg$_{fuel}$ g/kg$_{fuel}$

following the formulation of Unterstrasser and Gierens (2010a). Table 7 shows how this optical depth varies over time for each scenario. In all cases, the predominant optical depth increases with the soot emissions index, with the relative difference between scenarios increasing over time. Scaling the emitted soot by a factor 2 with respect to the baseline case (set to 0.02 g/kg$_{fuel}$) increases the 5-hour predominant optical depth by 10.5%. Further increasing in the soot emission index yields smaller increases in τ_{pre}, although we find no reversal in trend for EI$_{BC}$ up to 3 times the baseline value.

Aggregating these results, we find that doubling the soot emission index from the baseline case increases the peak ice mass by approximately 23% and delays the time at which the peak occurs by up to 8 hours. This translates to a larger climate impact. Reducing the amount of released soot particles could instead cut down the contrail-cirrus radiative forcing; halving the soot emission index decreases the optical depth after five hours by ~14%.

https://doi.org/10.5194/acp-2019-498
Preprint. Discussion started: 17 July 2019

Atmospheric Chemistry and Physics Discussions

Table 8. Impact of the soot emission index on the emission conversion factors in the upper troposphere

EI_{BC} (g/kg_{fuel})	ECF_{O_3}	ECF_{NO_x}	ECF_{HNO_3}	$ECF_{N_2O_5}$
0.01	0.0386	0.3108	0.0488	0.0028
	-5.35%*	-3.25%*	-27.80%*	-121.0%*
0.02	0.0408	0.3212	0.0676	-0.0133
	-	-	-	-
0.04	0.0428	0.3375	0.112	-0.0225
	+4.88%*	+5.08%*	+65.1%*	+69.2%*
0.06	0.0432	0.3467	0.144	-0.0363
	+5.68%*	+7.93%*	+113.0%*	+172.8%*

Values are computed 24 hours after emissions. The emission time was set to 8:00 AM.
* Relative changes with respect to the baseline values corresponding to a soot emission index of 0.02 g/kg_{fuel}

3.5.3 Influence of the engine soot emission index on chemical composition

In addition to changing the optical properties of the contrail, the soot emissions index affects the chemical impact of the plume. Table 8 shows how the 24-hour emissions conversion factors for ozone, NO_x, and NO_x reservoir species change between the scenarios described in section 3.5.2.

Impacts on ozone production are small, with an overall difference of ~10% between the low and high emissions scenario. NO_x is affected to a greater extent. The ice crystal surface area in the plume provides a surface for rapid, heterogeneous conversion of N_2O_5 to HNO_3. The descending, crystal-dense contrail therefore rapidly converts NO_x into reservoir forms, with the overall rate and extent of conversion increasing with the soot emissions index. At a soot emissions index of 0.06 g/g_{fuel}, HNO_3 concentrations are 113% greater after 24 hours than for the baseline case, while an emissions index of 0.01 g/kg_{fuel} yields an HNO_3 concentration 27.8% lower. We also find that concentrations of NO_x, corresponding to the overall NO_x "survival fraction", are greater after 24 hours with higher soot emissions indices.

Chemical species have an asymmetric profile across the contrail height. A greater aerosol surface area in the lower side of the plume leads to larger chemical rates through heterogeneous chemistry. The extent of the asymmetry depends on ice crystal microphysical parameters and therefore on meteorological conditions as well as aircraft parameters. Additional information is shown in the supplemental information.

3.5.4 Effects of stratospheric contrails

We carry out an additional simulation to quantify how the radiative and chemical impact of contrails is different when forming in the stratosphere. Although unlikely due to the dry conditions of the stratosphere, any contrails which survive the initial formation stage would be likely to persist for significant periods due to the low mixing rates in this region of the atmosphere.

We find that the low temperature lapse rate in the stratosphere leads to a greater contrail ice mass, with longer-lived and optically thicker contrails. The flat temperature profile leads to deeper supersaturated regions and thus increases the depth of the contrail, while greater wind shear and longer lifetimes cause the contrail to spread further horizontally. In the stratosphere, we find that contrails reach horizontal dimensions of 20 to 25 km compared to 15 to 20 km in the upper troposphere after 10 hours.

The nitric acid emission conversion factors are also greater compared to the tropospheric case. The ECF for HNO_3 can reach values above one as ambient, short-lived N_2O_5 is converted to long-lived HNO_3. A doubling of the soot emission index leads to a 12.2% and 23.6% increase in the HNO_3 and N_2O_5 perturbations respectively. The same change in emission causes an increase of the ozone perturbation per unit of NO_x emitted by 9.39%.

Aircraft-induced stratospheric cirrus clouds are found to have longer lifetimes and lead to a greater optical thickness compared to tropospheric altitudes. Heterogeneous chemistry on ice crystals gains greater importance at lower pressures and shifts the N_2O_5-HNO_3 local equilibrium. Further work is needed to quantify how stratospheric contrails might differ from those which form in the troposphere.

https://doi.org/10.5194/acp-2019-498
Preprint. Discussion started: 17 July 2019

Atmospheric Chemistry and Physics Discussions

4 Limitations and further work

Although our approach gives a significant improvement in terms of numerical fidelity compared to the instant dilution approach, additional work is needed to improve the simulation. For example, APCEMM accounts for mixing with ambient air and the effect of wind shear on the plume. However, it does not account for enhanced diffusion from the small-scale vortices generated by the wind shear. We also take a highly simplified approach to simulating the vertical motion of the plume due to radiative heating of the contrail. Future work is planned to explicitly model these processes in APCEMM.

These results are also isolated to the 24-hour period immediately following passage of an aircraft. In order to translate these results into an assessment of the net global impact of aviation, we aim to implement the results of the plume-scale processing of aircraft emissions into a global atmospheric chemistry-transport model.

5 Conclusions

We develop a parameterized aircraft plume model to simulate chemistry in an aircraft wake. This study shows that neglecting the non-linear plume-scale processes leads to inaccuracies in the assessment of O_3 perturbations and of the conversion of NO_x to reservoir species.

We use APCEMM to quantify the 24-hour atmospheric chemical response to aircraft emissions, and how it differs from the results simulated under the "instant-dilution" approach typically used in global models. We also assess how this depends on ambient conditions, aircraft parameters and fuel properties. Based on a parameter sweep for typical cruise conditions, we find that the instant dilution assumption leads to greater ozone production compared to the plume model, with errors of up to ~200% at cruise altitude. This is due to plume-scale effects not resolved in the instant-dilution apprach. In the plume model, the release of emissions into a small volume leads to O_3 depletion (through NO titration) and a HO_x-limited regime that last up to 5 hours after emissions. The lack of HO_x, which never occurs in the instant dilution approach, causes enhanced ozone production and a reduced fraction of NO_x remaining in the plume. We also quantify the role of wind shear and atmospheric diffusion.

Our approach also permits us to explicitly model the formation and effects of condensation trails. These affect the in-plume chemical response through heterogeneous reactions on the surface of ice crystals. Such plume-scale processes are not accounted for in almost all global-scale modeling approaches, but are needed in order to fully understand the role of aircraft particulate emissions in upper tropospheric chemistry. We find that a 50% reduction of the mass of emitted soot leads to a decrease of 65% in the aircraft-attributable HNO_3 perturbation, while ozone and nitrogen oxides are reduced by ~5% and 3% respectively. This is accompanied by a 14% decrease in the 5-hour optical depth of the contrail, the effects of which would not be captured in models which lack explicit plume modeling.

Previous studies assessing the impacts of aviation emissions have released emissions at the grid-scale level. We recommend that atmospheric models include a plume-scale treatment (or parameterization thereof) of aircraft emissions to compensate for these errors. Parameters should include meteorological conditions, local atmospheric composition, flight properties as well as engine and fuel characteristics. This is expected to significantly affect the estimated contribution of aircraft emissions to atmospheric NO_x and ozone.

Appendix A: Growth during the early plume phase

A1 Growth of ice particles during the early phase

As previously stated, the rate of change in the ice mass of a particle, m_p, is given by

$$\frac{dm_p}{dt} = H_p^{\mathrm{act}}(m_p) \times 4\pi C_p D_{\mathrm{v,eff}} \left(P_{\mathrm{H_2O}} - P_{\mathrm{H_2O}}^{\mathrm{sat}}\right), \tag{A1}$$

where $H_{\mathrm{p}}^{\mathrm{act}}$ is a function accounting for nucleus activation (equation A3), C_p is the ice crystal capacitance (equal to the particle radius r_p for spherical nuclei), $D_{\mathrm{v,eff}}$ is the effective water vapor diffusion coefficient in air (equation A4), and $P_{\mathrm{H_2O}}$ the water partial pressure.

The saturation vapor pressure of water $P_{\mathrm{H_2O}}^{\mathrm{sat}}$ is calculated as

$$P_{\mathrm{H_2O}}^{\mathrm{sat}} = \exp\left(r_K / r_p\right) \times P_{\mathrm{H_2O}}^{\mathrm{flat}} \tag{A2}$$

where r_p is the particle radius (in nm), r_K is the Kelvin radius (set here to 2.3 nm), and $P_{\mathrm{H_2O}}^{\mathrm{flat}}$ is the saturation vapor pressure over a flat surface. The factor $\exp(r_K/r_p)$ represents the effect of particle curvature (the Kelvin effect), increasing the apparent vapor

https://doi.org/10.5194/acp-2019-498
Preprint. Discussion started: 17 July 2019

Atmospheric Chemistry and Physics Discussions

pressure over a convex surface relative to a flat surface (Lewellen et al., 2014). p_{H_2O} is calculated as a function of temperature only (Pruppacher et al., 1998).

Growth is only permitted if particles are activated, meaning that they either already have an ice coating or in air which is locally supersaturated. This is characterized through the variable H_p^{act}, as

$$H_p^{\text{act}} = \begin{cases} 1 & \text{if } m_p > 0 \text{ or } \text{RH}_{w,\text{loc}} \geq 1 \\ 0 & \text{otherwise.} \end{cases} \tag{A3}$$

where $\text{RH}_{\text{w,loc}}$ is the local relative humidity with respect to liquid water (Picot et al., 2015). $D_{\text{v,eff}}$ accounts for latent heat effects, and is calculated as

$$D_{\text{v,eff}} = \frac{D_{\text{v}} \times \beta(r_p)}{\frac{D_{\text{v}} L_s P^{\text{sat}}_{\text{H}_2\text{O}}}{\kappa_d T}\left(\frac{L_s}{R_{\text{v}} T}\right) + R_{\text{v}} T}, \tag{A4}$$

where L_s is the latent heat of sublimation and κ_d the thermal conductivity of air. The function β accounts for the transition in uptake behavior between the gas kinetic ($\text{Kn} \gg 1$) to the diffusional regime ($\text{Kn} \to 0$), and is calculated as

$$\beta(r_p) = \left(\frac{1}{1 + r_p/\lambda_v} + \frac{2 D_{\text{v}} C_p}{\alpha v_{\text{th,v}} r_p^2}\right)^{-1} \tag{A5}$$

with α being the deposition coefficient. For deposition of water molecules on ice particles, we take $\alpha = 0.5$ which is in agreement with laboratory and field studies from Haag et al. (2003). The mean free-path of vapor molecules λ_v and the diffusion coefficient of vapor in air D_{v} are functions of the local temperature and pressure and are computed according to relations from Pruppacher et al. (1998).

A2 Growth of liquid particles during the early phase

In the early plume phase, liquid particles form as the plume undergoes rapid cooling. As stated previously, we use the parameterization from Vehkamäki et al. (2002) to compute nucleation rates, cluster size and composition.

Throughout the plume lifetime, the growth of liquid particles is affected by coagulation, which dominates the early-plume phase because of the initially high aerosol concentrations. Coagulation is a volume-conserving process that decreases the aerosol number concentration.

Coagulation of newly-formed aerosols and scavenging by soot and ice particles take place on different timescales. The coagulation timescale of particles of radius r_1 can be evaluated from $t_{\text{coa}} = 1/(\text{K}(r_1, r_2) n_2)$, where n_2 and r_2 are the number density and the radius of the scavenging particles. As shown in the supplementary information, self-coagulation of liquid aerosols (r_1 = 0.5 - 10 nm) occurs on a timescale of a few seconds to minutes, assuming a typical number density between 10^6 and 10^{10} particles/cm^3. Similarly, scavenging by soot and ice particles happens over timescales that are of the same order of magnitude, assuming a radius of 50 nm (1 µm) for soot particles (for ice crystals, respectively) and a number density of 10^3 molecules/cm^3. On the other hand, self-aggregation of soot particles and ice crystals occur on timescales that are much longer, of the order of several hours.

Appendix B: Coagulation kernel

The coagulation kernel represents Brownian diffusion, convective Brownian diffusion enhancement, sedimentation-induced aggregation, and turbulent inertial motion, as well as enhancement due to turbulent shear. The kernel is described by the following equations, taken from Jacobson (2005). We here consider a particle of size i coagulating with particles of size j.

The Brownian collision kernel is described by:

$$\text{K}^{\text{B}}_{i,j} = \frac{4\pi(r_i + r_j)(D_{p,i} + D_{p,j})}{\frac{r_i + r_j}{r_i + r_j + \sqrt{\delta_i^2 + \delta_j^2}} + \frac{4(D_{p,i} + D_{p,j})}{\sqrt{\bar{v}_{p,i}^2 + \bar{v}_{p,j}^2}(r_i + r_j)}}, \tag{B1}$$

where r is the particle radius, D_p the particle diffusion coefficient, δ the mean distance from the center of a sphere reached by particles leaving the sphere's surface and traveling a distance equal to the particle mean free path and $\bar{v}_p$ the thermal speed of a particle in air.

https://doi.org/10.5194/acp-2019-498
Preprint. Discussion started: 17 July 2019

Atmospheric Chemistry and Physics Discussions

The convective Brownian diffusion enhancement kernel is defined by:

$$K_{i,j}^{DE} = \begin{cases} K_{i,j}^{B} 0.45 Re_j^{1/3} Sc_{p,i}^{1/3} & \text{if } Re_j \leq 1,\ r_j \geq r_i \\ K_{i,j}^{B} 0.45 Re_j^{1/2} Sc_{p,i}^{1/3} & \text{if } Re_j > 1,\ r_j \geq r_i, \end{cases} \tag{B2}$$

where Re and Sc are the particle Reynolds and Schmidt numbers.

The sedimentation-induced aggregation kernel is described by:

$$K_{i,j}^{SI} = E_{coll,i,j} \pi (r_i + r_j)^2 \mid V_{f,i} - V_{f,j} \mid, \tag{B3}$$

where E_{coll} is a collision efficiency.

The turbulent inertial motion and turbulent shear kernel are defined by:

$$K_{i,j}^{TI} = \frac{\pi \varepsilon_d^{3/4}}{g \nu_a^{1/4}} (r_i + r_j)^2 \mid V_{f,i} - V_{f,j} \mid \tag{B4}$$

$$K_{i,j}^{TS} = \left(\frac{8\pi\varepsilon_d}{15\nu_a} \right)^{1/2} (r_i + r_j)^3, \tag{B5}$$

where ε_d is the rate of dissipation of turbulent kinetic energy, g the acceleration due to gravity and ν_a the kinematic viscosity.

The total coagulation kernel is equal to the sum of each individual kernel:

$$K_{i,j} = K_{i,j}^{B} + K_{i,j}^{DE} + K_{i,j}^{SI} + K_{i,j}^{TI} + K_{i,j}^{TS}. \tag{B6}$$

Appendix C: Plume-averaged NO_x chemical rate

We assume that the conversion of NO_x to reservoir species is dictated by the daytime conversion pathway through the following reactions:

$$NO_2 + OH \xrightarrow{M} HNO_3 \tag{CR1}$$

$$NO_2 + HO_2 \xrightarrow{M} HO_2NO_2 \tag{CR2}$$

The chemical reaction rate can be written as:

$$\frac{d[NO_2]}{dt} = -(k_1[OH] + k_2[HO_2])[NO_2]$$

$$\frac{d[NO_2]}{dt} = -k_{eff}[HO_x][NO_2]$$

where HO_x has been defined such that $[HO_x] = \frac{k_1[OH]+k_2[HO_2]}{k_1+k_2}$.

We assume that the concentration field at a fixed point can be expressed as the sum of spatially-averaged quantity and the instantaneous fluctuation, such that:

$$[NO_2] = \overline{[NO_2]} + [NO_2]'$$

$$[HO_x] = \overline{[HO_x]} + [HO_x]'$$

The chemical conversion rate of NO_x can therefore be written as:

$$\begin{aligned} \frac{d\overline{[NO_2]}}{dt} &= -k_{eff} \times \overline{[HO_x][NO_2]} \\ &= -k_{eff} \times \left(\overline{[HO_x]} \times \overline{[NO_2]} + \overline{[HO_x]' \times [NO_2]'} \right) \end{aligned}$$

https://doi.org/10.5194/acp-2019-498
Preprint. Discussion started: 17 July 2019

Atmospheric Chemistry and Physics Discussions

The first term on the right hand side leads to a net depletion. NO_2 is an emitted species. Therefore, the NO_2 fluctuation is positive in the core of the plume, while it is negative far away. HO_x, however, gets depleted to form HNO_3 and HO_2NO_2. Therefore, $[HO_x]' \leq 0$ in the inner plume and $[HO_x]' \geq 0$ outside of the core. Thus, the second term reduces NO_x conversion and is proportional to the correlation of the fluctuations. If both fluctuations are negatively correlated, the depletion is reduced compared the case where the fields are uniform.

This explains why, for the same emission quantity, a small plume with large spatial fluctuations leads to a lower conversion compared to a large plume with smaller gradients.

Author contributions. T.M.F. implemented and ran the model, and wrote the manuscript. All authors were involved in study design, model validation and improvement, and manuscript review, editing, and finalization.

Competing interests. The authors declare no competing interests.

Acknowledgements. This work was supported by NASA grant number NNX14AT22A.

References

Airbus: Global market forecast 2017-2036, https://www.airbus.com/aircraft/market/global-market-forecast.html, 2017.

Beard, K. V. and Ochs III, H. T.: Collisions between small precipitation drops. Part II: Formulas for coalescence, temporary coalescence, and satellites, Journal of the atmospheric sciences, 52, 3977–3996, 1995.

Boeing: Commercial Market Outlook 2018-2037, https://www.boeing.com/commercial/market/commercial-market-outlook, 2017.

Brasseur, G., Cox, R., Hauglustaine, D., Isaksen, I., Lelieveld, J., Lister, D., Sausen, R., Schumann, U., Wahner, A., and Wiesen, P.: European scientific assessment of the atmospheric effects of aircraft emissions, Atmospheric Environment, 32, 2329–2418, 1998.

Brasseur, G. P., Müller, J.-F., and Granier, C.: Atmospheric impact of NOx emissions by subsonic aircraft: A three-dimensional model study, Journal of Geophysical Research: Atmospheres, 101, 1423–1428, 1996.

Cariolle, D., Caro, D., Paoli, R., Hauglustaine, D., Cuenot, B., Cozic, A., and Paugam, R.: Parameterization of plume chemistry into large-scale atmospheric models: Application to aircraft NOx emissions, Journal of Geophysical Research: Atmospheres, 114, 2009.

Damian, V., Sandu, A., Damian, M., Potra, F., and Carmichael, G. R.: The kinetic preprocessor KPP-a software environment for solving chemical kinetics, Computers & Chemical Engineering, 26, 1567–1579, 2002.

Dürbeck, T. and Gerz, T.: Dispersion of aircraft exhausts in the free atmosphere, Journal of Geophysical Research: Atmospheres, 101, 26 007–26 015, 1996.

Eastham, S. D. and Barrett, S. R.: Aviation-attributable ozone as a driver for changes in mortality related to air quality and skin cancer, Atmospheric Environment, 144, 17–23, 2016.

Eastham, S. D., Weisenstein, D. K., and Barrett, S. R.: Development and evaluation of the unified tropospheric–stratospheric chemistry extension (UCX) for the global chemistry-transport model GEOS-Chem, Atmospheric Environment, 89, 52–63, 2014.

Ebert, E. E. and Curry, J. A.: A parameterization of ice cloud optical properties for climate models, Journal of Geophysical Research: Atmospheres, 97, 3831–3836, 1992.

Eyring, V., Stevenson, D. S., Lauer, A., Dentener, F. J., Butler, T., Collins, W. J., Ellingsen, K., Gauss, M., Hauglustaine, D. A., Isaksen, I. S., et al.: Multi-model simulations of the impact of international shipping on atmospheric chemistry and climate in 2000 and 2030, Atmospheric Chemistry and Physics, 7, 757–780, 2007.

Forstall, W. and Shapiro, A. H.: Momentum and mass transfer in coaxial gas jets, JOURNAL OF APPLIED MECHANICS-TRANSACTIONS OF THE ASME, 17, 399–408, 1950.

Gottlieb, D. and Orszag, S. A.: Numerical analysis of spectral methods: theory and applications, vol. 26, Siam, 1977.

Gupta, K., Rehman, A., and Sarviya, R.: Bio-fuels for the gas turbine: A review, Renewable and Sustainable Energy Reviews, 14, 2946–2955, 2010.

Haag, W., Kärcher, B., Ström, J., Minikin, A., Lohmann, U., Ovarlez, J., and Stohl, A.: Freezing thresholds and cirrus cloud formation mechanisms inferred from in situ measurements of relative humidity, Atmospheric Chemistry and Physics, 3, 1791–1806, 2003.

Heymsfield, A. J., Lawson, R. P., and Sachse, G.: Growth of ice crystals in a precipitating contrail, Geophysical Research Letters, 25, 1335–1338, 1998.

Iwabuchi, H., Yang, P., Liou, K., and Minnis, P.: Physical and optical properties of persistent contrails: Climatology and interpretation, Journal of Geophysical Research: Atmospheres, 117, 2012.

Jacobson, M.: Numerical solution to drop coalescence/breakup with a volume-conserving, positive-definite, and unconditionally stable scheme, Journal of the Atmospheric Sciences, 68, 334–346, 2011.

Jacobson, M. Z.: Development and application of a new air pollution modeling system—II. Aerosol module structure and design, Atmospheric Environment, 31, 131–144, 1997.

https://doi.org/10.5194/acp-2019-498
Preprint. Discussion started: 17 July 2019

Atmospheric Chemistry and Physics Discussions

Jacobson, M. Z.: Development of mixed-phase clouds from multiple aerosol size distributions and the effect of the clouds on aerosol removal, Journal of Geophysical Research: Atmospheres, 108, 2003.

Jacobson, M. Z.: Fundamentals of atmospheric modeling, Cambridge university press, 2005.

Jacobson, M. Z., Turco, R. P., Jensen, E. J., and Toon, O. B.: Modeling coagulation among particles of different composition and size, Atmospheric Environment, 28, 1327–1338, 1994.

Jaecker-Voirol, A. and Mirabel, P.: Heteromolecular nucleation in the sulfuric acid-water system, Atmospheric Environment (1967), 23, 2053–2057, 1989.

Jensen, E. J., Ackerman, A. S., Stevens, D. E., Toon, O., Minnis, P., et al.: Spreading and growth of contrails in a sheared environment, Journal of Geophysical Research: Atmospheres, 103, 31 557–31 567, 1998.

Jung, J. G., Pandis, S. N., and Adams, P. J.: Evaluation of nucleation theories in a sulfur-rich environment, Aerosol Science and Technology, 42, 495–504, 2008.

Kärcher, B.: A trajectory box model for aircraft exhaust plumes, Journal of Geophysical Research: Atmospheres, 100, 18 835–18 844, 1995.

Kärcher, B.: Physicochemistry of aircraft-generated liquid aerosols, soot, and ice particles-1. Model description, Journal of Geophysical Research-Atmospheres, 103, 17 111–17 128, 1998.

Kärcher, B.: Aviation-produced aerosols and contrails, Surveys in geophysics, 20, 113–167, 1999.

Kärcher, B.: Formation and radiative forcing of contrail cirrus, Nature communications, 9, 1824, 2018.

Kärcher, B., Hirschberg, M., and Fabian, P.: Small-scale chemical evolution of aircraft exhaust species at cruising altitudes, Journal of Geophysical Research: Atmospheres, 101, 15 169–15 190, 1996.

Kärcher, B., Busen, R., Petzold, A., Schröder, F., Schumann, U., and Jensen, E.: Physicochemistry of aircraft-generated liquid aerosols, soot, and ice particles: 2. Comparison with observations and sensitivity studies, Journal of Geophysical Research: Atmospheres, 103, 17 129–17 147, 1998.

Kärcher, B., Burkhardt, U., Unterstrasser, S., and Minnis, P.: Factors controlling contrail cirrus optical depth, Atmospheric Chemistry and Physics, 9, 6229–6254, 2009.

Kärcher, B., Burkhardt, U., Bier, A., Bock, L., and Ford, I.: The microphysical pathway to contrail formation, Journal of Geophysical Research: Atmospheres, 120, 7893–7927, 2015.

Kraabøl, A. G., Konopka, P., Stordal, F., and Schlager, H.: Modelling chemistry in aircraft plumes 1: comparison with observations and evaluation of a layered approach, Atmospheric environment, 34, 3939–3950, 2000.

Lee, J. J., Lukachko, S. P., Waitz, I. A., and Schafer, A.: Historical and future trends in aircraft performance, cost, and emissions, Annual Review of Energy and the Environment, 26, 167–200, 2001.

Lewellen, D., Meza, O., and Huebsch, W.: Persistent contrails and contrail cirrus. Part I: Large-eddy simulations from inception to demise, Journal of the Atmospheric Sciences, 71, 4399–4419, 2014.

Mazraati, M.: World aviation fuel demand outlook, OPEC energy review, 34, 42–72, 2010.

Meijer, E., Velthoven, P., Thompson, A., Pfister, L., Schlager, H., Schulte, P., and Kelder, H.: Model calculations of the impact of NO x from air traffic, lightning, and surface emissions, compared with measurements, Journal of Geophysical Research: Atmospheres, 105, 3833–3850, 2000.

Meijer, E. W.: Modelling the impact of subsonic aviation on the composition of the atmosphere, Technische Universiteit Eindhoven, 2001.

Minnis, P., Young, D. F., Garber, D. P., Nguyen, L., Smith, W. L., and Palikonda, R.: Transformation of contrails into cirrus during SUCCESS, Geophysical Research Letters, 25, 1157–1160, 1998.

Napari, I., Noppel, M., Vehkamäki, H., and Kulmala, M.: Parametrization of ternary nucleation rates for H2SO4-NH3-H2O vapors, Journal of Geophysical Research: Atmospheres, 107, 2002.

Paoli, R., Vancassel, X., Garnier, F., and Mirabel, P.: Large-eddy simulation of a turbulent jet and a vortex sheet interaction: particle formation and evolution in the near field of an aircraft wake, Meteorologische Zeitschrift, 17, 131–144, 2008.

Penner, J. E.: Aviation and the global atmosphere: a special report of the Intergovernmental Panel on Climate Change, Cambridge University Press, 1999.

Petry, H., Hendricks, J., Möllhoff, M., Lippert, E., Meier, A., Ebel, A., and Sausen, R.: Chemical conversion of subsonic aircraft emissions in the dispersing plume: Calculation of effective emission indices, Journal of Geophysical Research: Atmospheres, 103, 5759–5772, 1998.

Picot, J., Paoli, R., Thouron, O., and Cariolle, D.: Large-eddy simulation of contrail evolution in the vortex phase and its interaction with atmospheric turbulence, Atmospheric Chemistry and Physics, 15, 7369–7389, 2015.

Pruppacher, H. R., Klett, J. D., and Wang, P. K.: Microphysics of clouds and precipitation, 1998.

Schumann, U.: The impact of nitrogen oxides emissions from aircraft upon the atmosphere at flight altitudes—results from the AERONOX project, Atmospheric Environment, 31, 1723–1733, 1997.

Schumann, U.: A contrail cirrus prediction model, Geoscientific Model Development, 5, 543–580, 2012.

Schumann, U., Konopka, P., Baumann, R., Busen, R., Gerz, T., Schlager, H., Schulte, P., and Volkert, H.: Estimate of diffusion parameters of aircraft exhaust plumes near the tropopause from nitric oxide and turbulence measurements, Journal of Geophysical Research: Atmospheres, 100, 14 147–14 162, 1995.

Schumann, U., Schlager, H., Arnold, F., Baumann, R., Haschberger, P., and Klemm, O.: Dilution of aircraft exhaust plumes at cruise altitudes, Atmospheric Environment, 32, 3097–3103, 1998.

https://doi.org/10.5194/acp-2019-498
Preprint. Discussion started: 17 July 2019

Atmospheric Chemistry and Physics Discussions

Schumann, U., Schlager, H., Arnold, F., Ovarlez, J., Kelder, H., Hov, Ø., Hayman, G., Isaksen, I., Staehelin, J., and Whitefield, P. D.: Pollution from aircraft emissions in the North Atlantic flight corridor: Overview on the POLINAT projects, Journal of Geophysical Research: Atmospheres, 105, 3605–3631, 2000.

Schumann, U., Arnold, F., Busen, R., Curtius, J., Kärcher, B., Kiendler, A., Petzold, A., Schlager, H., Schröder, F., and Wohlfrom, K.-H.: Influence of fuel sulfur on the composition of aircraft exhaust plumes: The experiments SULFUR 1–7, Journal of Geophysical Research: Atmospheres, 107, 2002.

Seidel, D. J., Free, M., and Wang, J.: Diurnal cycle of upper-air temperature estimated from radiosondes, Journal of Geophysical Research: Atmospheres, 110, 2005.

Song, C., Chen, G., Hanna, S., Crawford, J., and Davis, D.: Dispersion and chemical evolution of ship plumes in the marine boundary layer: Investigation of O3/NOy/HOx chemistry, Journal of Geophysical Research: Atmospheres, 108, 2003.

Speth, R. L., Rojo, C., Malina, R., and Barrett, S. R.: Black carbon emissions reductions from combustion of alternative jet fuels, Atmospheric Environment, 105, 37–42, 2015.

Tabazadeh, A., Jensen, E. J., and Toon, O. B.: A model description for cirrus cloud nucleation from homogeneous freezing of sulfate aerosols, Journal of Geophysical Research: Atmospheres, 102, 23 845–23 850, 1997.

Tang, M., Cox, R., and Kalberer, M.: Compilation and evaluation of gas phase diffusion coefficients of reactive trace gases in the atmosphere: volume 1. Inorganic compounds, Atmospheric Chemistry and Physics, 14, 9233–9247, 2014.

Toon, O. B. and Miake-Lye, R. C.: Subsonic aircraft: Contrail and cloud effects special study (SUCCESS), Geophysical Research Letters, 25, 1109–1112, 1998.

Tremmel, H., Schlager, H., Konopka, P., Schulte, P., Arnold, F., Klemm, M., and Droste-Franke, B.: Observations and model calculations of jet aircraft exhaust products at cruise altitude and inferred initial OH emissions, Journal of Geophysical Research: Atmospheres, 103, 10 803–10 816, 1998.

Unterstrasser, S.: Properties of young contrails–a parametrisation based on large-eddy simulations, Atmospheric Chemistry and Physics, 16, 2059–2082, 2016.

Unterstrasser, S. and Gierens, K.: Numerical simulations of contrail-to-cirrus transition–Part 1: An extensive parametric study, Atmospheric Chemistry and Physics, 10, 2017–2036, 2010a.

Unterstrasser, S. and Gierens, K.: Numerical simulations of contrail-to-cirrus transition–Part 2: Impact of initial ice crystal number, radiation, stratification, secondary nucleation and layer depth, Atmospheric Chemistry and Physics, 10, 2037–2051, 2010b.

Unterstrasser, S., Gierens, K., and Spichtinger, P.: The evolution of contrail microphysics in the vortex phase, Meteorologische Zeitschrift, 17, 145–156, 2008.

Unterstrasser, S., Gierens, K., Sölch, I., and Wirth, M.: Numerical simulations of homogeneously nucleated natural cirrus and contrail-cirrus. Part 2: Interaction on local scale, Meteorol. Z, pp. 1–19, 2016.

Unterstrasser, S., Gierens, K., Sölch, I., and Lainer, M.: Numerical simulations of homogeneously nucleated natural cirrus and contrail-cirrus. Part 1: How different are they?, Meteorologische Zeitschrift, 26, 621–642, 2017.

Vehkamäki, H., Kulmala, M., Napari, I., Lehtinen, K. E., Timmreck, C., Noppel, M., and Laaksonen, A.: An improved parameterization for sulfuric acid–water nucleation rates for tropospheric and stratospheric conditions, Journal of Geophysical Research: Atmospheres, 107, 2002.

Vinken, G. C., Boersma, K. F., Jacob, D. J., and Meijer, E. W.: Accounting for non-linear chemistry of ship plumes in the GEOS-Chem global chemistry transport model, Atmospheric Chemistry and Physics, 11, 11 707–11 722, 2011.

Vohralik, P., Randeniya, L., Plumb, I., and Baughcum, S.: Effect of plume processes on aircraft impact, Journal of Geophysical Research: Atmospheres, 113, 2008.

Wong, H.-W. and Miake-Lye, R.: Parametric studies of contrail ice particle formation in jet regime using microphysical parcel modeling, Atmospheric Chemistry and Physics, 10, 3261–3272, 2010.